Influence of the scar geometry on landslide dynamics and deposits: Application to Martian landslides

Antoine Lucas,[1,2] Anne Mangeney,[1] Daniel Mège,[3] and François Bouchut[4]

Received 24 January 2011; revised 23 June 2011; accepted 30 June 2011; published 4 October 2011.

[1] Landslides dynamics prediction remains difficult in spite of a considerable number of studies. The runout distance is widely used in analysis of landslide dynamics and in the calibration of the rheological parameters involved in numerical modeling. However, the unknown impact of the significant uncertainty in the shape of the initial released mass on the runout distance and on the overall shape of the deposit raises questions about the relevance of these approaches. The impact of the initial scar geometry on flow and distribution of the deposits is studied here using satellite data and numerical modeling of theoretical landslides, and Martian landslides informed by geomorphological analysis, by varying the initial scar geometry from spoon-shaped to steep wall geometry. Our results show that the runout distance is a very robust parameter that is only slightly affected by the change in the geometry of the initial scar. On the contrary, the lateral extent of the deposit is shown to be controlled by the scar geometry, providing unique insights into the initial landsliding conditions on Mars and makes it possible to accurately recover the volume initially involved, an essential ingredient for volume balance calculation. A feedback analysis of Valles Marineris landslides can be drawn, showing good agreement between numerical results and geomorphological analysis; the geometry of the initial scar inferred from numerical modeling is strongly correlated with the regional tectonic history in Valles Marineris area.

Citation: Lucas, A., A. Mangeney, D. Mège, and F. Bouchut (2011), Influence of the scar geometry on landslide dynamics and deposits: Application to Martian landslides, *J. Geophys. Res.*, *116*, E10001, doi:10.1029/2011JE003803.

1. Introduction

[2] Landslides, debris flows and avalanches sculpt the surface morphology on Earth as well as on other planets. They constitute one of the most efficient weathering processes currently active on Mars [*Malin et al.*, 2006; *Schorghofer et al.*, 2007]. On Earth, mass failure results in the destruction of human lives and infrastructures.

[3] Many studies have been carried out to understand the mechanics of landslides. Experimental and numerical modeling of granular flows have provided some clues through the development of scaling laws and theoretical models to quantify landslide dynamics and the morphology of their deposits [e.g., *Voellmy*, 1955; *Cruden and Hungr*, 1986; *Savage and Hutter*, 1989; *Hungr*, 1995; *Cruden and Varnes*, 1996; *Iverson*, 1997; *Dade and Huppert*, 1998; *Pouliquen*, 1999; *Legros*, 2002; *Kerswell*, 2005; *Roche et al.*, 2004; *Mangeney-Castelnau et al.*, 2003; *Félix and Thomas*, 2004; *Mangeney-Castelnau et al.*, 2005; *Phillips et al.*, 2006; *Pirulli et al.*, 2007; *Pudasaini and Hutter*, 2007; *Mangeney et al.*, 2007a; *Hungr*, 2008]. Whereas laboratory experiments have helped in identifying rheological properties and establishing scaling laws relating the deposit and the flow dynamics [*Pouliquen*, 1999; *Pouliquen and Forterre*, 2002; *Lube et al.*, 2004; *Lajeunesse et al.*, 2004; *Siavoshi and Kudrolli*, 2005; *Phillips et al.*, 2006; *Pudasaini and Hutter*, 2007; *Mangeney et al.*, 2010], numerical modeling have been useful to extrapolate and apply these rheological properties to field observations as well as to provide insight into the parameters involved in the observed scaling laws [*Iverson et al.*, 2004; *Mangeney-Castelnau et al.*, 2005; *Kerswell*, 2005; *Hogg*, 2008; *Mangeney et al.*, 2007a, 2007b; *Lucas and Mangeney*, 2007; *Lacaze et al.*, 2008; *Favreau et al.*, 2010; *Mangold et al.*, 2010].

[4] Landslide dynamics strongly depend on the underlying topography, on the geometry and volume of the released mass, on the nature and mechanical behavior of the flowing material [e.g., *Hungr*, 1995; *Denlinger and Iverson*, 2001, 2004; *Harrison and Grimm*, 2003; *Mangeney-Castelnau et al.*, 2003, 2005; *Lucas and Mangeney*, 2007; *Pudasaini and Hutter*, 2007; *Sosio et al.*, 2008; *Favreau et al.*, 2010]. However, none of these parameters are well constrained. The runout distance, i.e., the maximum distance reached by the landslide, has been extensively used to calibrate friction coefficients in numerical models of landslide dynamics [e.g., *Lucas and Mangeney*, 2007; *Pirulli and Mangeney*, 2008]

[1]Institut de Physique du Globe de Paris, Université Paris Diderot, UMR CNRS 7154, Paris, France.
[2]Now at Division of Geological and Planetary Sciences, California Institute of Technology, Pasadena, California, USA.
[3]Laboratoire de Planétologie et de Géodynamique, Université de Nantes, UMR CNRS 6112, Nantes, France.
[4]Laboratoire d'Analyse et de Mathématiques Appliquées, Université Paris-Est, UMR CNRS 8050, Marne la Vallèe, France.

0148-0227/11/2011JE003803

and to establish scaling laws relating the morphometry of the deposit to the initial characteristics of the released mass [*Lube et al.*, 2004; *Lajeunesse et al.*, 2004; *Mangeney-Castelnau et al.*, 2005; *Mangeney et al.*, 2010]. In particular, the so-called mobility of landslide is calculated using measurements of the runout distance [e.g., *Legros*, 2002; *Lucas and Mangeney*, 2007].

[5] When comparing experimental and numerical results with field data, the question however remains as to whether the runout distance of real landslides depends on the geometry of the initial scar that is difficult to measure in the field due to erosion and insufficient accuracy of the available topography data. The upper surface of the released mass can be reconstructed through extrapolation of the relief surrounding the scar. On the contrary, the bottom of the scar is generally hidden by the landslide deposits or eroded by subsequent events. What is the effect of the uncertainty on initial scar geometry on the calibration of rheological parameters in numerical models? Does it change the scaling laws relating the characteristics of the deposit to the initial conditions?

[6] The unknown geometry of the scar bottom makes it difficult to assess the initial volume of the released mass on Martian as well as on terrestrial landslides. The volume involved in landsliding is, however, a crucial input in numerical models and in the calculation of global mass balance in areas subjected to mass wasting. Furthermore, the difference in volume between the initial (pre-failure) and final mass (post-failure) has been used to draw conclusions about the emplacement processes on Mars. For example, *Quantin et al.* [2004] found a decrease in volume between the initial released mass and the final deposit for the about 50 landslides observed in Valles Marineris on Mars and inferred the presence of thermokarst, implying lenses of ice in the initial rock. On the contrary, *Sato et al.* [2007] found an increase in volume using the same data set. These opposite conclusions show the large uncertainty in volume calculation which, in these examples, is greater than the difference between the initial and the final volume, excluding any realistic mass balance calculations and thus interpretation on initial conditions.

[7] There are very few data on natural landslides that can help clarify these questions. The main issue is to find several landslides in the same geological context but with different initial conditions. Actually, the difference in the topography and in the material involved in various places on Earth hides the potential effect of the initial scar geometry on landslide dynamics and deposits. In this respect, the landslides (about fifty) observed in exploration probe imagery of Valles Marineris on Mars provide a unique paradigm to study the effect of initial scar geometry [*Lucchitta*, 1978, 1979, 1987]. The topography is quite simple and homogeneous all along the valley; landslides are generated by mass failure in the canyon wall and the debris flow over almost flat bedrock. The deposits are easily identified through satellite data analysis due to the small erosion rate and the absence of vegetation. Furthermore, the data resolution on Mars is high enough in comparison to the size of the events.

[8] Landsliding in Valles Marineris has important implications for climatic and hydrologic conditions. Triggering mechanisms and emplacement processes have been debated based on geomorphological, experimental and numerical studies [*Lucchitta*, 1979, 1987; *McEwen*, 1989; *Shaller*, 1991; *Legros*, 2002; *Harrison and Grimm*, 2003; *Quantin et al.*, 2004; *Soukhovitskaya and Manga*, 2006; *Lucas and Mangeney*, 2007]. Some studies have argued in favor of hydrated conditions for landsliding to occur [*Lucchitta*, 1978, 1979, 1987; *Shaller et al.*, 1989], whereas others argue in dry conditions [*McEwen*, 1989; *Soukhovitskaya and Manga*, 2006; *Lajeunesse et al.*, 2006]. In any case, several studies have shown a very high mobility of Martian landslides [*Lucchitta*, 1979, 1987; *Lucchitta et al.*, 1992; *Melosh* 1979; *Shaller*, 1991; *Legros*, 2002; *Harrison and Grimm*, 2003; *Quantin et al.*, 2004; *Lucas and Mangeney*, 2007].

[9] The question here is to assess if the uncertainty in scar geometry can challenge or support the previous conclusions on volume change between initial state and final deposits and on the high mobility of Valles Marineris landslides. This issue is addressed using satellite data imagery and numerical modeling of granular flows over complex topography.

[10] After a brief description of the numerical model used in this study in section 2, estimation of the effect of initial scar geometry on the dynamics and deposits of granular flows as well as on volume estimation is performed on theoretical 2-D and 3-D geometry (section 3). Finally, in section 4 simulations of four Martian landslides are performed and the effect of the uncertainty in the initial scar geometry on landslide dynamics and mobility is discussed in relation to the local geological context, in particular to challenge previous conclusions regarding landslide emplacement mechanisms.

2. Numerical Model Description

[11] Simulation is performed using the numerical model SHALTOP developed through a collaboration between Département de Mathématiques et Applications (DMA), École Normale Supérieure (ENS, Paris), and Institut de Physique du Globe de Paris (IPGP). SHALTOP describes granular flows over complex 3-D topography [*Bouchut et al.*, 2003; *Bouchut and Westdickenberg*, 2004; *Mangeney-Castelnau et al.*, 2005; *Mangeney et al.*, 2007a]. The model is based on the depth-averaged thin layer approximation (i.e., the flow is supposed to be thin compared to its length) and takes into account a Coulomb-type friction law following the pioneering approach of *Savage and Hutter* [1989]. It describes the change in time of the thickness $h(x, y)$ and of the depth-averaged velocity of the flow $\mathbf{u}(x, y)$ along the topography. Contrary to most of the models used in geophysics, this model deals with the full tensor of terrain curvature that appears in the momentum equations when the asymptotic development is rigorously handled. The equations solved in the model are detailed in the Appendix A.

[12] Debris avalanche is treated here as a single-phase, dry granular flow with Coulomb-type behavior, involving a friction coefficient μ (see Appendix A for details on the friction force). The friction coefficient is here supposed to be constant, i.e., Coulomb friction law:

$$\mu = \tan\delta, \tag{1}$$

where δ is the constant friction angle. A more complex flow rule is also implemented in this model (also known as *Pouliquen law*) involving a friction coefficient $\mu(h, u)$

Table 1. Summary of Geomorphic Data for Large Martian Landslides[a]

Site	H_i (km)	L_i (km)	a	R_f (km)	H_f (m)	δ (deg)
			This Study[b]			
Coprates	4.4 ± 0.5	10.5 ± 1.2	0.42 ± 0.22	48.9 ± 2	2483 ± 130	7.2
Ius	5.8 ± 0.4	12.9 ± 0.6	0.45 ± 0.12	43.3 +?	2351 ± 160	8.2
Ophir	4.9 ± 0.2	10.8 ± 0.3	0.45 ± 0.07	41.5 ± 2	3001 ± 200	9.8
Ganges	3.7 ± 0.4	7.2 ± 0.8	0.51 ± 0.22	40.5 ± 3	2131 ± 130	7
			Other Examples[c]			
North Coprates[d]	6.6 ± 1	11.1 ± 2	0.59 ± 0.33	61.9 ± 4	–	–
East Ius	5.9 ± 0.4	15 ± 2	0.39 ± 0.20	39.1 ± 3	–	–
Ganges 2	4.9 ± 0.3	9.9 ± 0.8	0.49 ± 0.14	35.5 ± 2	–	–
Ganges 3	3.6 ± 0.4	6.8 ± 0.8	0.52 ± 0.22	30.6 ± 2	–	–

[a]H_i is initial height, L_i initial length, a is the initial aspect ratio ($a = H_i/L_i$), $R_f = \Delta L = L_f - L_i$ the final runout length, and H_f is the estimated difference between the highest point of deposits lying on the scar and the deepest point below the deposits inside the scar. The friction angle δ is the optimal one found in simulations. Uncertainties are calculated from resolution of the data and estimated errors involved in interpretation.
[b]The upper group corresponds to simulated landslides in this study.
[c]The bottom group contains other examples taken at different areas on which topographic reconstruction has not been performed.
[d]North Coprates is mentioned in Figure 9 and East Ius is mentioned in Figure 6.

widely used in applied physics (see Appendix A and D). Although this law has been successful in reproducing experimental granular flows and some natural landslides [e.g., *Pouliquen and Forterre*, 2002; *Lucas et al.*, 2007; *Mangeney et al.*, 2007a; *Pirulli and Mangeney*, 2008; *Mangold et al.*, 2010], its use is difficult because of the high number of involved empirical parameters. In contrast, the Coulomb friction law only involves one empirical parameter, the friction angle δ, making the use of this law very simple as no constitutive equations are currently available for granular media.

[13] The relevance of thin-layer modeling using a Coulomb friction law to describe granular collapse has been previously tested by comparing SHALTOP with discrete element simulations and experiments on the collapse of granular columns over an horizontal plane by varying the initial aspect ratio of the granular column [*Mangeney-Castelnau et al.*, 2005; *Mangeney et al.*, 2006]. The main result is that depth-averaged models fail to reproduce the dynamics of granular spreading if the aspect ratio of the initial released mass is greater than about 1. In that case, vertical acceleration has to be included in the model. Nevertheless, for natural landslides considered here the initial aspect ratio ranges from $a = 0.42$ to $a = 0.51$ (see Table 1) so that the thin layer approach is appropriate for our study.

[14] Moreover, SHALTOP can successfully reproduce the dynamics and the deposits shape of granular avalanches across irregular three-dimensional terrain [*Lucas et al.*, 2008] after experimental tests performed by *Iverson et al.* [2004]. This model has been also able to reproduce self-channeling flows over an inclined bed with levees formations [*Mangeney et al.*, 2007a], as well as natural landslides [*Lucas and Mangeney*, 2007; *Lucas et al.*, 2008; *Kuo et al.*, 2009; *Mangold et al.*, 2010]. Furthermore, *Favreau et al.* [2010] have shown that SHALTOP is able to reproduce complex time-dependent basal stress fields applied on top of a complex terrain by comparing actual seismic records with the simulated seismic waves calculated from the "landslide source" obtained with the model SHALTOP. This last study also showed that curvature effects play a major role in this stress field and therefore in landslide dynamics.

3. Theoretical Flow and Scar Geometries

[15] Simple synthetic topography has been used to assess the influence of the initial scar geometry on granular flow dynamics and deposits without dealing with the full natural complexity.

3.1. 2-D Granular Flow

[16] Slumping of a 2-D granular mass is investigated here. Three initial scar geometries are defined: the parabolic scar, an inclined scar made of an inclined plane followed by an horizontal plane, and a box-like scar with a vertical wall and horizontal floor (see Figures 1a, 1b, and 1c, respectively). The "box" geometry corresponds to the release of a rect-

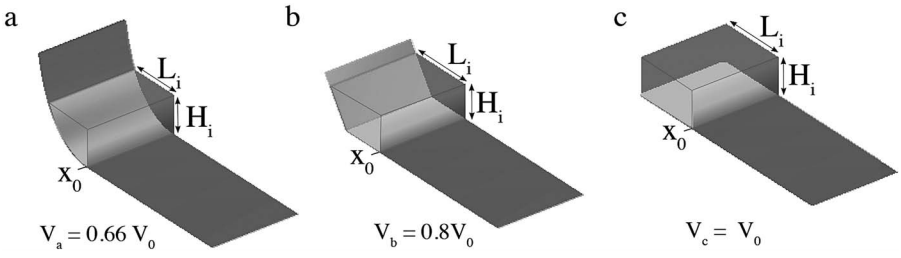

Figure 1. 2-D theorical geometries hereafter named (a) "parabola," (b) "inclined," and (c) "box." The initial mass is indicated in transparency over topography. H_i is the initial height, L_i the initial mass length, x_o the position of the initial front and V_i is respective volume with $V_0 = 204$ km^3.

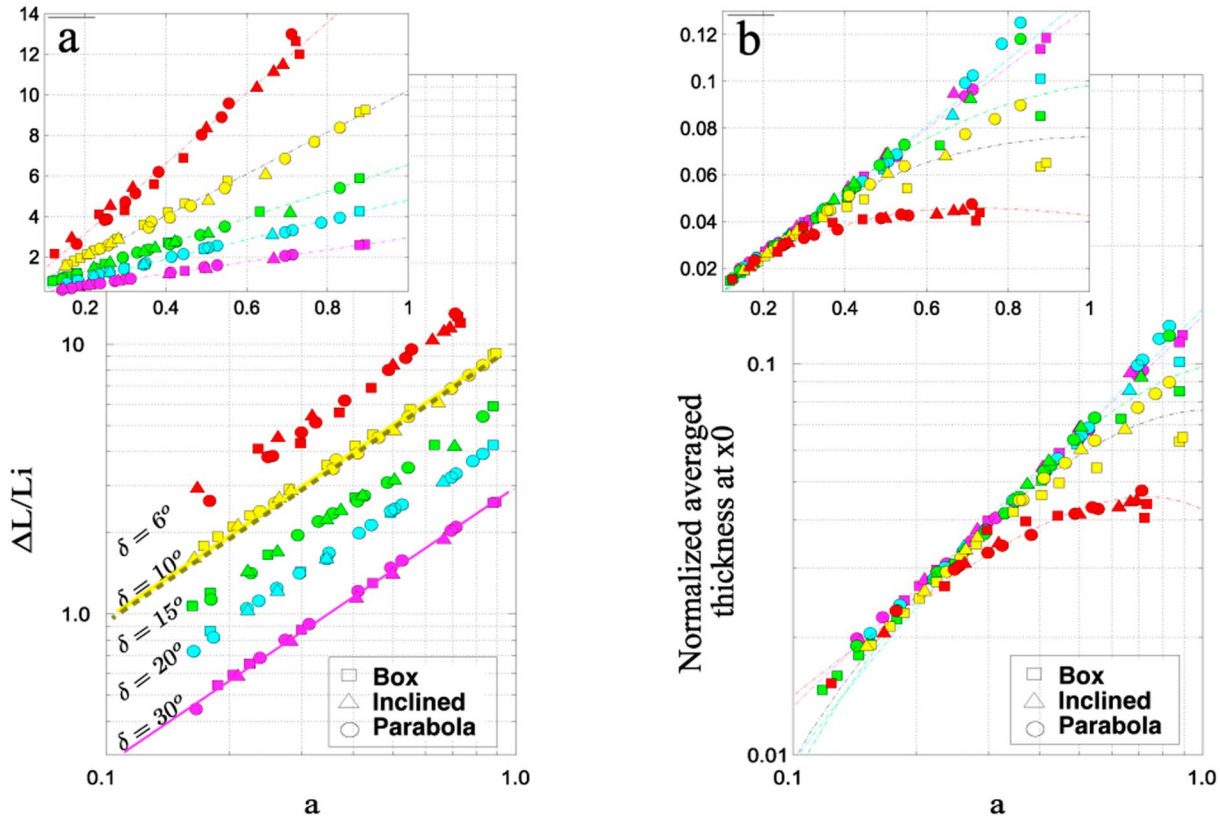

Figure 2. Scaling laws on the deposit characteristics obtained for the three 2-D scar geometries "parabola," "inclined," and "box" dealing with the friction angle $\delta \in [6°, 30°]$. (a) Normalized runout $\Delta L/L_i$ as function of initial aspect ratio $a = H_i/L_i$. For $\delta = 10°$ and 30° curves calculated from equation (2) were added (bold lines) with $\gamma = 1.7$: The yellow line corresponds to $\delta = 10°$ and $\theta = 0°$, the brown dashed line corresponds to $\delta = 12°$ and $\theta = 2°$ and the purple line corresponds to $\delta = 30°$ and $\theta = 0°$. (b) Normalized thickness (taken at $x = x_0$, see Figure 1) as a function of initial aspect ratio a.

angular column of granular material over an horizontal or inclined plane, similar to the setting of recent laboratory experiments and numerical studies [e.g., *Hogg*, 2008; *Hungr*, 2008; *Mangeney et al.*, 2010]. The parabolic geometry is generally assumed for natural scars and the inclined scar geometry lies in between the two others.

[17] The characteristic dimensions of the scars are of the order of the natural scars of Martian landslides ($H_i \simeq 3$ km). The initial aspect ratio varies from 0.16 to 0.89 and the volume of the initial released mass is $V_{box} = 204$ km^3, $V_{inclined} = 168$ km^3 ($0.8 \times V_{box}$), and $V_{parabolic} = 135$ km^3 ($0.66 \times V_{box}$), for the wall, inclined and parabolic like scar geometry, respectively. Indeed, changing the scar geometry while keeping the upper surface of the released mass constant, induces a change in the released volume. The geometry of the upper surface of the granular mass has been shown to change the runout distance reached by the mass for granular collapse over an horizontal plane [see *Mangeney-Castelnau et al.*, 2005, Figure 8]. However, in natural landslides the surface geometry of the released mass is quite well constrained by the lateral borders of the apparent scar and by the surrounding topography so that it is kept constant in this sensitivity study (see section 4.2.2).

[18] Using an analytical solution of the granular dam-break problem [*Mangeney et al.*, 2000] and experimental results, *Lucas and Mangeney* [2007] and *Mangeney et al.* [2010] suggest a simple relation linking the normalized runout distance to the initial aspect ratio of the released mass:

$$\frac{\Delta L}{L_i} = \frac{\gamma a}{\tan\delta - \tan\theta} \tag{2}$$

where L_i is the initial length of the rectangular released mass, the initial aspect ratio defined as $a = H_i/L_i$, θ is the mean slope angle of the bottom topography, $\Delta L = Ł_f - L_i$ is the runout and $\gamma \simeq 1$ is an empirical parameter.

[19] Figure 2a shows the relation between normalized runout $\Delta L/L_i$ and initial aspect ratio a for a range of friction angles $\delta \in [6°, 30°]$ using the 3 different geometries. Our simulations show that the linear relation (2) between the normalized runout distance and the initial aspect ratio is still observed for all tested geometries of the initial scar and for all considered friction angles. As the friction angle gets smaller, slight changes of the runout distance are observed when the geometry of the initial scar changes. The maximum difference in the simulated runout is about 7%, obtained with $\delta = 6°$ and $a = 0.72$. Surprisingly, the runout

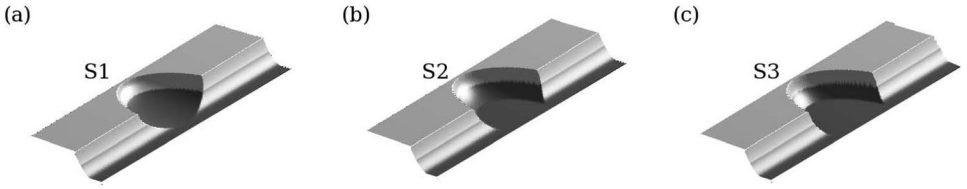

Figure 3. Tested scar geometry named S_i, i = [1, 3] for (a) the spoon-seated, (b) the intermediate, and (c) the wall-seated geometry, respectively. The plateau surrounds the floor over 3 km (see Figure 5). The higher the i, the steeper the scar geometry. Induced volumes are respectively $V_3 = 128\%\ V_1$, $V_2 = 115\%\ V_1$ with $V_1 = 135\ \text{km}^3$ for aspect ratio $a = 0.31$.

distance is almost insensitive to the geometry of the initial scar. As a result, the runout distance is shown to be a very robust parameter. This strong result could be related to what is observed in the analytical solution for dam-break granular problem [*Mangeney et al.*, 2000; *Kerswell*, 2005; *Hogg*, 2008]. Actually, analytical solutions of hyperbolic equations for thin granular flows show that the perturbation of the flow behind the front never reaches the moving front. The changes in the flow induced by the scar geometry located behind the front is then expected not to catch up with the front and thus will not affect the runout distance.

[20] The mean thickness is calculated here by taking into account the deposit from the initial position of the front (noted x_0 in Figure 1), to the final runout distance. In this manner, we only compare parts of the deposit under which the geometries are the same for each case.

[21] Figure 2b presents the normalized averaged thickness (calculated at x_o) as a function of the initial aspect ratio a for a range of friction angle $\delta \in [6°, 30°]$ using the 3 different geometries. Obviously, the lower the friction angle, the thinner the final deposit due to increasing runout distance. This mean thickness of the deposit is more affected than the runout distance by the change in the initial scar geometry. For $\delta = 6°$, the initial scar geometry only slightly affect the mean thickness of the deposits. More sensitivity of the mean thickness of the deposit to the scar geometry is observed for $\delta = 10°$, $\delta = 15°$ and $\delta = 20°$. The effect of the initial scar geometry on the mean thickness of the deposit is stronger when the aspect ratio of the granular mass increases. The mean deposit thickness appears to be smaller for the wall scar geometry than for the parabolic scar whereas the released volume is bigger for the wall scar case. Most of the volume excess in this latter case remains within the source area. Indeed, the downslope gravity acceleration is greater for a parabolic scar than for the wall scar for which gravity acceleration along the scar bottom is equal to zero.

3.2. 3-D Granular Flows

[22] Unconfined tests are now performed in order to investigate the influence of the initial geometry of the scar on the 3-D deposit shape and particularly on the lateral spreading.

[23] Three schematic scar geometries are considered (Figures 3a–3c). The first geometry (S_1) involves a conic scar with rounded lateral walls hereafter called spoon-seated. The third geometry (S_3) corresponds to a cylindric scar with steep lateral walls, called deep-seated whereas the second geometry (S_2) lies in between the two others. The characteristic dimensions of the scar are of the same order of magnitude of those of Martian landslides (H_i = 3 km and 0.3 km < L_i < 0.66 km). Obviously, the volume of the initial mass changes with the shape of the scar geometry. The wall-like scar implies a volume about 28% larger (V_3 = 172.8 km^3) than for the parabolic scar (V_1 = 135 km^3), while the second scar geometry involves a volume 15% larger (V_2 = 155.25 km^3) than the parabolic scar. For the three geometries, the wall edges on both sides of the scar have been smoothed using a parabolic equation in order to avoid numerical problems that would result from sharp variations of the topography.

[24] Scaling laws obtained for 3-D tests are shown in Figure 4. Normalized runout as a function of the initial aspect ratio with friction angles δ = [12°, 2°] confirms the 2-D results. The runout distance is only weakly affected by the difference in the initial scar geometry (Figure 4a). The observed runouts for S_3 and S_2 is only $\simeq$13% greater than the runout simulated using the scar geometry S_1. This is an important result suggesting that the usual way of fitting friction coefficients on runout distance is quite reasonable even if the initial scar geometry is not well known. Indeed, by increasing the friction angle δ by 0.8° for the scar geometry S_1 is enough to simulate the same runout distance as that calculated with S_2 and S_3. In other words, the errors in the definition of the scar geometry will generate an error of 1° on the friction angle obtained by back-analysis of the runout distance.

[25] Moreover, the normalized deposit area is also marginally affected by the shape of the scar and seems to only depend on the friction angle and initial aspect ration (Figure 4b). On the other hand, the maximum width and therefore the overall shape of the deposit are clearly controlled by the scar geometry (Figure 4c).

[26] As suggested by equation (2), decreasing the friction angle will act in a quite similar way as increasing the slope of the bottom topography, especially for small slope and friction angles where $\tan\phi \simeq \phi$, for $\phi = \delta, \theta$. Indeed, the shape and runout distance simulated with $\theta = 2°$ and $\delta = 12°$ (Figures B1g–B1i in Appendix B) almost correspond to the values calculated with $\theta = 0°$ and $\delta = 10°$ (Figures B1j–B1l in Appendix B). However, lateral spreading is larger for this last group of simulations (see Figures B1j–B1l in Appendix B).

[27] As a result, in this range of inclination and friction angles, considering a flat topography leads to an error in the friction angle obtained by back analysis of the observed deposit, almost equal to the real slope angle, here 2°. As already suggested by *Lucas and Mangeney* [2007], topography effects (slope of the bottom topography and scar

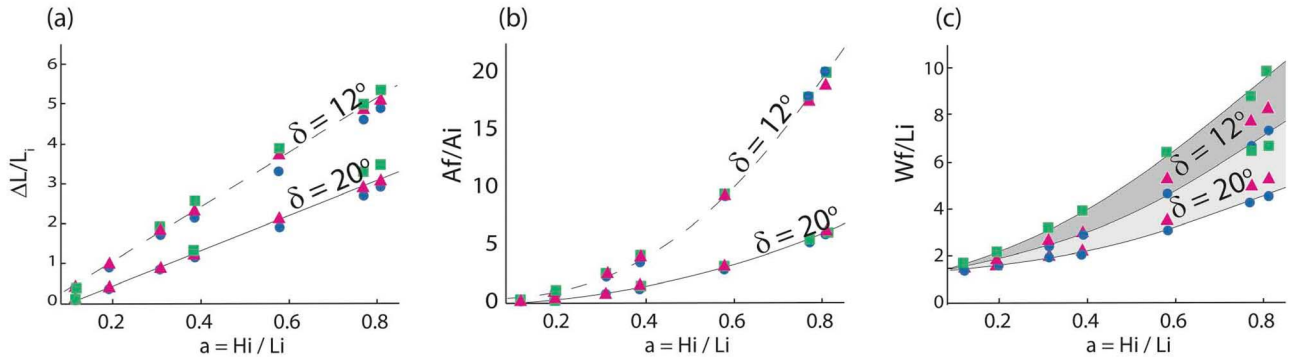

Figure 4. Scaling laws on the deposit characteristics obtained from 3-D tests for S_1 scar (blue circles), S_2 scar (pink triangles), and S_3 (green squares). (a) Normalized runout ($\Delta L/L_i$) as a function of the initial aspect ratio ($a = H_i/L_i$) for each S_i, i = [1, 3] dealing with friction angle $\delta = 12°$ (dashed curve) and $\delta = 20°$ (plain curve). (b) Ratio of the final area A_f to the initial area A_i as a function of initial aspect ratio a for each S_i, i = [1, 3] and two friction angles $\delta = 12°$ (dashed curve) and $\delta = 20°$ (plain curve). (c) Final width of deposits over initial length (which is here equal to initial width) as a function of initial aspect ratio a obtained for each S_i, i = [1, 3]. Dark gray trend is for $\delta = 12°$ and light gray trend is for $\delta = 20°$.

geometry) are far too small to explain the difference in the effective friction coefficient required to simulate experimental granular flows ($\delta \sim 30°$) and natural Martian landslides ($\delta \sim 9°$).

[28] Interestingly the thickness profile taken at the middle of the deposits, i.e. in the main flow direction, is also only slightly affected by the shape of the scar (Figure 5).

[29] In contrast, the lateral extent of the deposit is strongly dependent on the scar geometry, ranging from a lobe shape for the parabolic scar to an arrow-like shape for the wall scar. The excess in volume from S_1 to S_3 seems to be distributed mainly in the lateral direction (i.e., perpendicular to the flow direction and to the steepest slope). The lateral extent of the deposit gets closer to the value of the runout distance as the scar geometry gets steeper and deeper. These results show that information on the shape of the initial scar geometry and thus on the initial volume involved can be deduced from the observation of the deposit shape.

[30] Moreover, the different deposit shapes (ranging from a lobe to an arrow-like shape) observed in these theoretical simulations correspond to the deposit shapes of Martian landslides (Figure 6). Note that similarly to what has been observed in 2-D, the upper part of the scar is more exposed for a smooth parabolic scar than for a wall scar (compare Figures 6 and B1 in Appendix B). For natural cases, this feature is difficult to observe as slight variations of friction angle as well as Toreva blocks (a distinctive feature observed upstream of some landslides deposits [*Reiche*, 1937; *Kelfoun and Druitt*, 2005]) could influence the degree of scar exposure.

[31] In addition, our simulations suggest that parabolic scars will be drained more efficiently during slumping than deep-seated scars and thus less covered by landslide deposits. This is consistent with the observation showing that landslides with smooth scars are expected to reveal a significant portion of the upper part of their scar.

[32] As a result, the 3-D landslide deposit shapes observed on Mars (e.g., in the Valles Marineris area) might carry the signature of the shape of the initial scar geometry, possibly related to different triggering mechanisms, as will be discussed in detail in the following section.

4. Application to Martian Landslides

4.1. Landslides and Geological Context

[33] The four Martian landslides studied here (Figures 7 and 8) are located in Valles Marineris, a series of large

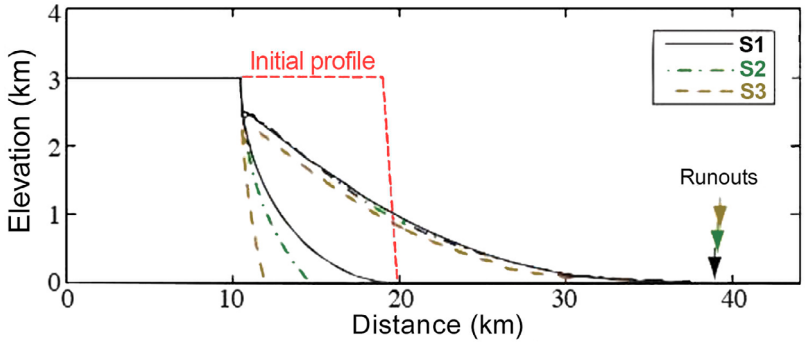

Figure 5. Cross sections of simulated deposit thickness $h(x)$ for the three scar geometry tested S_1, S_2, and S_3. Arrows indicate the runout for each case.

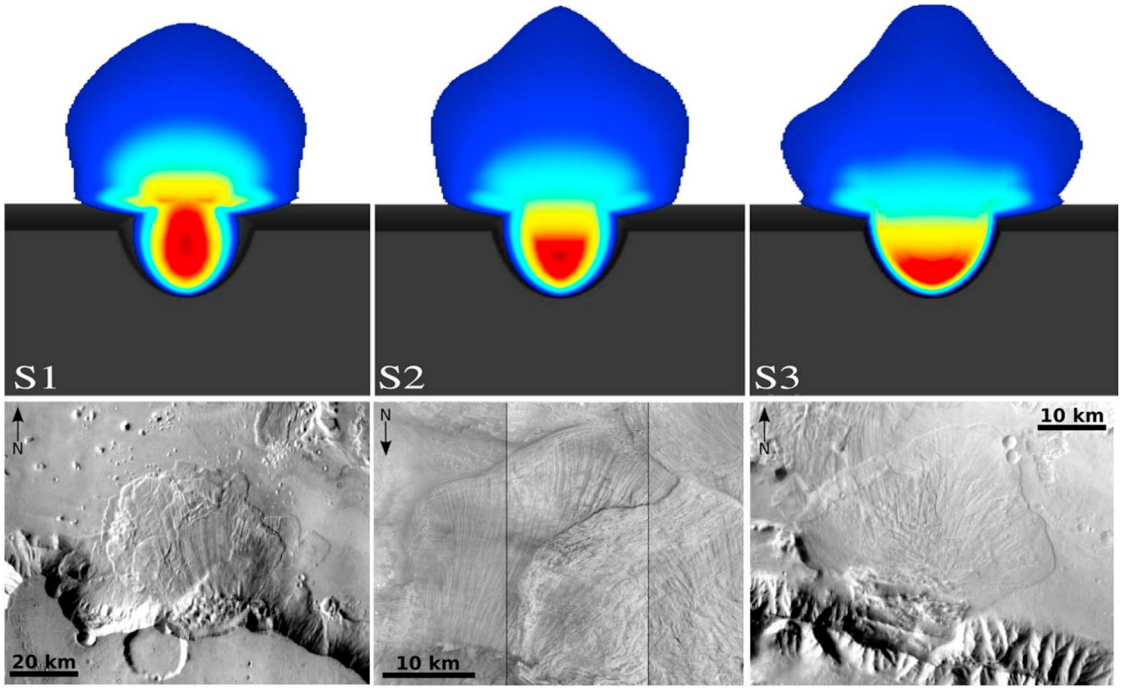

Figure 6. (top) Deposits of simulated landslides obtained for each scar geometry S_i using $\delta = 10°$. (bottom) Martian landslides observed on THEMIS IR present similar deposit shapes, respectively, from left to right: Ganges Chasma, East Ius Chasma, and Coprates Chasma.

troughs (chasmata) cutting a thinly stratified plateau of probable volcanic composition [*McEwen*, 1989; *Christensen et al.*, 2003]. The similar lithology and geologic setting of the investigated landslides minimizes the influence of local geological peculiarities on flow dynamics and deposits. These landslides (Coprates Chasma, Ius Chasma, Ophir Chasma, and Ganges Chasma) have been selected because of their easily identifiable deposits. In addition, no topographic obstructions are seen to have interfered with the runout of the landslides.

[34] Actually in contrary to most observed landslides, the landslides in Coprates Chasma, Ophir Chasma and Ganges Chasma, do not reach the opposite wall within the valley (Figures 8a, 8c, and 8d). Ius Chasma is deviated by topography barriers (Figure 8b). All these landslides are the result of slope failure in the canyon wall, generating mass flow along the canyon floor, down a gentle slope of a few degrees (typically ~2°). As shown by *Peulvast et al.* [2001], some areas in Valles Marineris are clearly controlled by normal faulting whereas some others do not present evi-

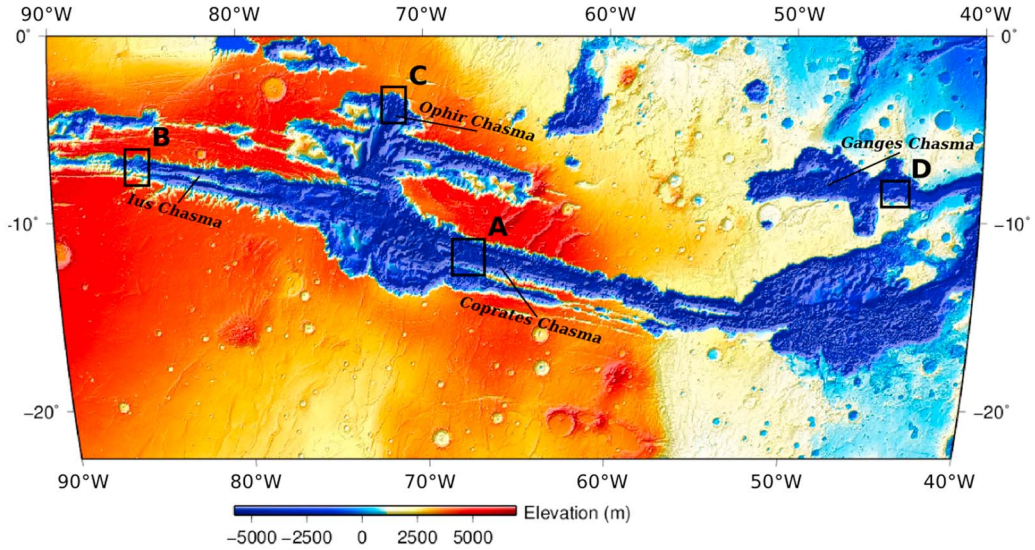

Figure 7. Valles Marineris topographic map (from MOLA data). Black boxes indicate the landslides occurring in the different Chasma, shown just below on daytime THEMIS IR mosaics in Figure 8.

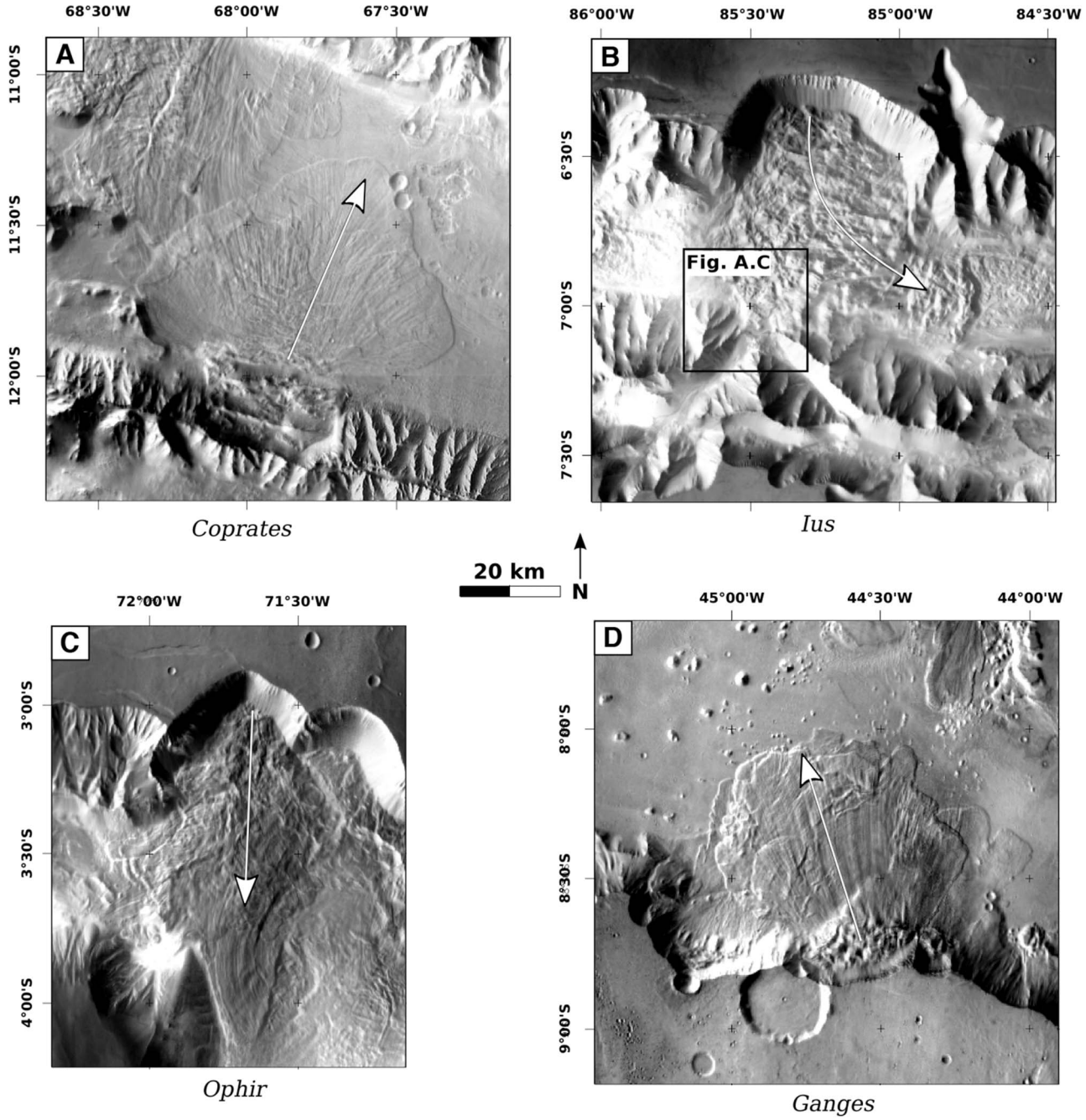

Figure 8. THEMIS IR images of studied landslides (a) Coprates Chasma, (b) Ius Chasma, (c) Ophir Chasma, and (d) Ganges Chasma. White arrows indicate the mean flow direction. Light comes from the west. Black box in Figure 8b corresponds to Figure C1 in Appendix C.

dence of tectonic control. Two landslides in each context, i.e. Coprates and Ius Chasma in the normal faulting context and Ophir and Ganges Chasma in the other context, have been studied here and are detailed below. Quantitative information estimated from satellite imagery on the length L_i and thickness H_i of the initial released mass, on the deposit area A_f, and on the runout distance ΔL (i.e. maximum distance of the deposit front from the source area) are given for each landslide:

[35] 1. The Coprates Chasma landslide is located at 67°W and 12°S (Figure 8a). Coprates Chasma is a 5 ± 0.2 km deep graben, and landsliding occurred at the expense of a horst [*Schultz*, 1991; *Peulvast and Masson*, 1993; *Mège and Masson*, 1996; *Peulvast et al.*, 2001]. Runout length is ΔL = 49 km and the surface area covered by the landslide material is A_f = 2300 km^2. The initial height of the involved mass is estimated to be H_i = 4.4 ± 0.5 km and the initial length L_i = 10.5 ± 1.2 km, resulting in an initial aspect ratio $a = H_i/L_i$ = 0.42 (see Table 1). The landslide deposit includes a Toreva block (noted TB) and debris aprons (noted DA) downstream (Figure 9). *Reiche* [1937] proposed that Toreva blocks may occur when a stronger material

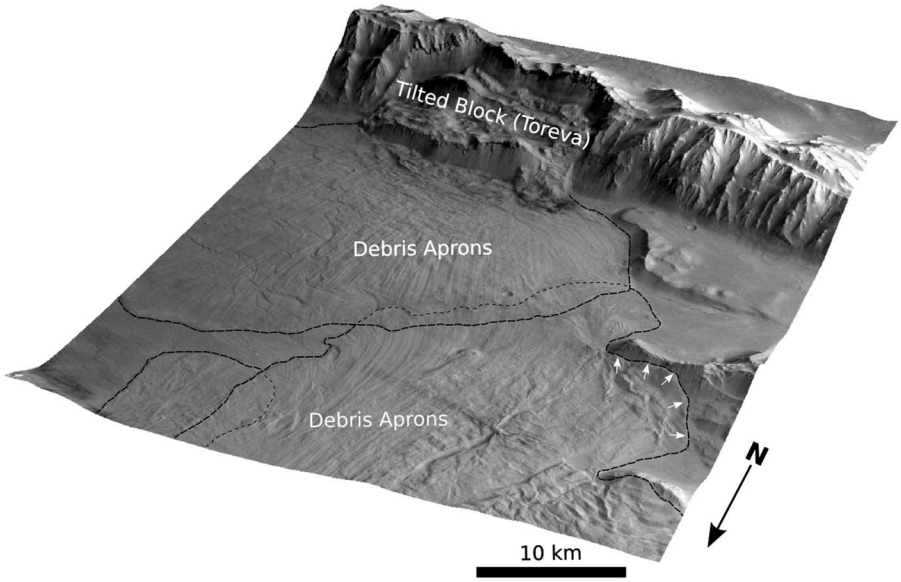

Figure 9. Southward perspective view of Coprates landslide showing debris aprons overlapping and tilted blocks (also called Toreva block). The wallslopes of each side of the scar are characterized by spur-and-gully morphologies. White arrows indicate evidence of a former landslide, coming from the north, that overcame the topographic relief up to 800 m, suggesting highly energetic flows (HRSC image).

overlies a weaker material, a hypothesis difficult to check in the Martian context [*Bigot-Cormier and Montgomery*, 2007]. Due to the presence of these Toreva blocks, the shape of the bottom scar is hidden. The chasma floor displays thinly stratified infilling (Figure 10) whose erosional patterns suggest a weaker lithology than the plateau material [e.g., *Peulvast and Masson*, 1993]. The floor on the eastern side of the debris aprons displays repeated bands of alternating reflectance (Figure 10) that are especially well displayed on THEMIS thermal infrared imagery (see section 4.2.1). These layers may either consist of moraines deposited along the path of a former valley glacier, or gently folded, stratified floor material with a fold axis parallel to the graben trend.

[36] 2. The Ius Chasma landslide occurred in the Ius trough (86°W and 5°S) which is bounded by fault-controlled walls with straight and well-aligned trend, similar to Coprates Chasma [*Peulvast et al.*, 2001] (Figure 8b). The Ius landslide runout distance does not exceed $\Delta L = 50$ km but the deposits overlay the opposite wallslope, making this value shorter than it would have been without topographic confinement. A diversion of the flow toward the east is observed probably due to the fact that the apron reached the opposite wallslope. The deposits area is estimated to $A_f = 1520$ km^2. The initial height of the involved mass is estimated to be $H_i = 5.8 \pm 0.4$ km and the initial length $L_i = 12.9 \pm 0.6$ km; i.e., an aspect ratio $a = 0.45$ (Table 1).

[37] 3. Ophir Chasma is located in the northern part of the central region of Valles Marineris (72°W and 3°S) (Figure 8c). The wallslopes of this chasma present less evidence of faulting than Ius and Coprates chasmata. The studied landslide shows a runout length of 45.5 ± 0.2 km with a deposit area of 1 330 km^2. The initial height of the involved mass is about $H_i = 4.9 \pm 0.2$ km and the initial length $L_i = 10.8 \pm 0.3$ km, i.e. an aspect ratio $a = 0.45$ (Table 1). Furthermore, *Lucas and Mangeney* [2007] have shown that deposits of Ophir landslide overlap a previous event coming from the north-east [see *Lucas and Mangeney*, 2007, Figure 2].

[38] 4. The Ganges Chasma landslide is located at 45°W and 8°S (Figure 8d). Ganges trough is shallow and shows smoother wallslopes without a clear structural trend. Runout length reaches 48.8 km and the deposit surface area is 1 670 km^2. The initial height of the involved mass is about $H_i = 3.7 \pm 0.4$ km and the initial length $L_i = 7.2 \pm 0.8$ km, i.e., an aspect ratio $a = 0.51$ (Table 1). The upper part of the scar is clearly more open-ended than those of Ius and Coprates landslides and does not appear to be fault-controlled (Figure 8d). Like Coprates, the Ganges landslide has Toreva blocks, making the failure geometry slightly harder to reconstruct.

[39] Each example here is treated as a single-event as we consider one event for one scar. This point is discussed in section 4.3.

[40] For all the landslides, the morphology of the chasma walls prior to landslide failure has been described as spurs-and-gullies. This morphology may form under a variety of possible conditions [*Lucchitta et al.*, 1992]. Locally, triangular faceted spurs are observed on the horst slope, whose lowest part is occupied by a weathered continuous fault scarp (see Figure 9 and *Peulvast et al.* [2001]).

4.2. Data and Processing

[41] For mass balance calculations between initial mass failure and final deposits as well as for inputs in numerical modeling, the topography before the landslide, the initial scar geometry and the shape of the initial released mass have to be reconstructed from the observations (Figure 11). Satellite data are used here to identify the landslide deposits (visible and infra-red imagery data) and to reconstruct Digital Topography Models (DTM) of the pre-failure and post-failure topography as well as of the initial scar geom-

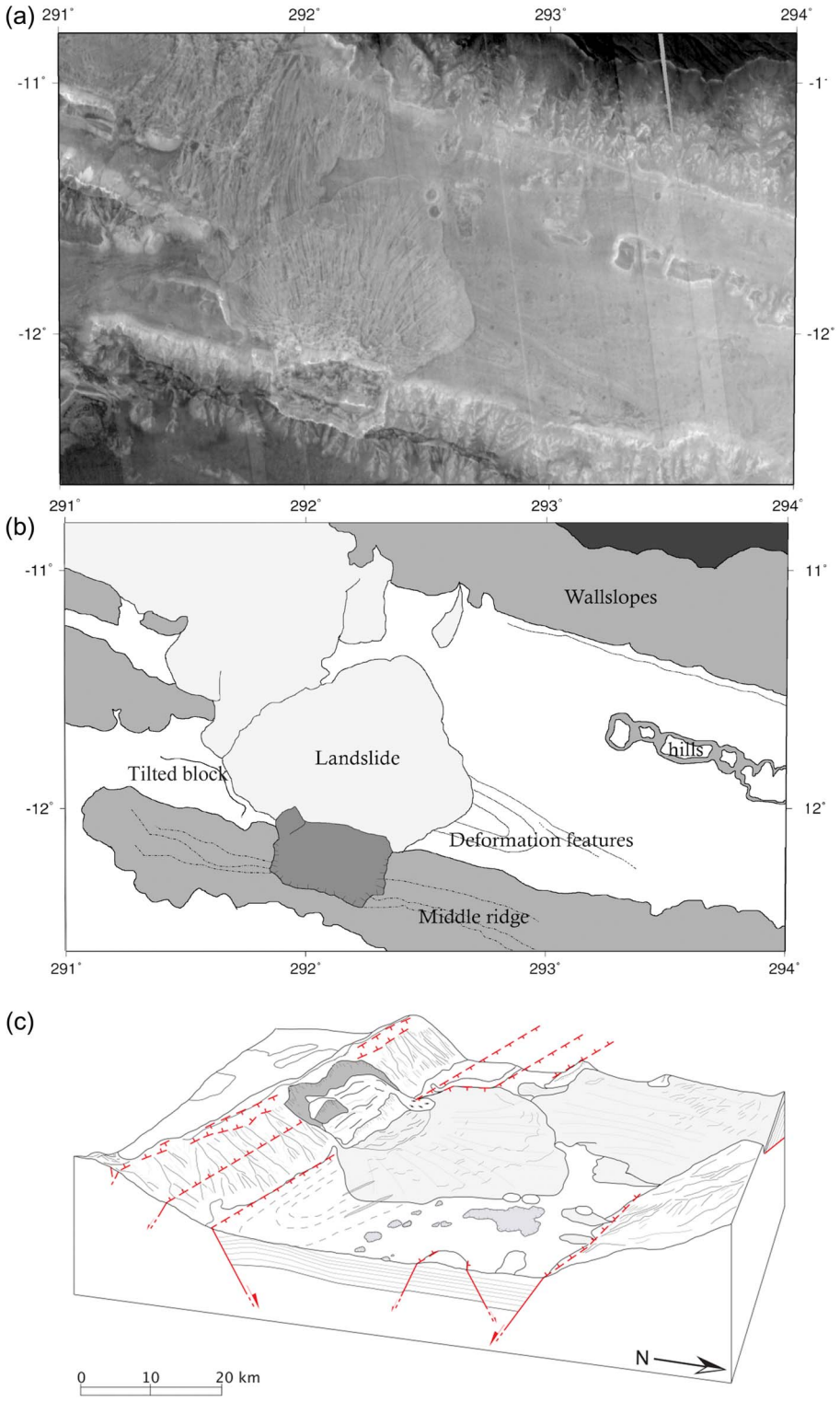

Figure 10. (a) Nighttime IR THEMIS map of Coprates Chasma. (b) Simplified structural map of Coprates Chasma. (c) Structural sketch of Coprates Chasma landslide. Uphill-facing scars on the tops of the ridge and anti-slope faults (dashed lines) are here interpreted as deep-seated context for the Coprates landslide.

etry of the released mass (laser topography data and stereo imagery).

[42] During the last decade, US and European Martian missions brought back an abundance of new data of high spatial precision. The Martian landslides are larger than similar landslides on Earth; in proportion, their topography is known with a precision which is in the same range as the one of the terrestrial landslides.

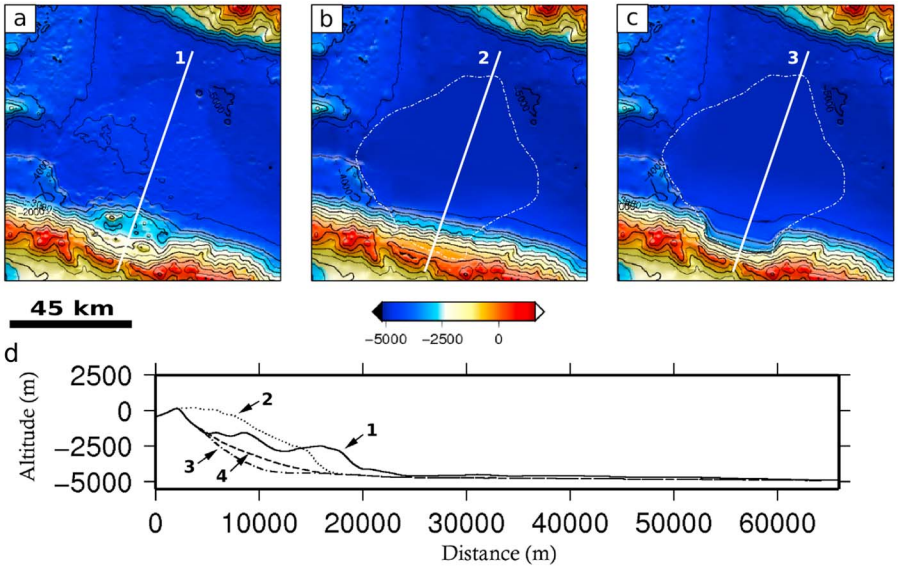

Figure 11. Stages of the DTM reconstruction pipeline. (a) MOLA topography of the landslide deposits of Coprates. (b) Reconstructed pre-event DTM. (c) Reconstructed deep-seated scar geometry. White dashed lines indicate the deposit outline identified from imagery. The full white line represents the location of (d) the profiles: profile 1 corresponds to the MOLA topography in Figure 11a, profile 2 corresponds to the pre-event topography in Figure 11b, profile 3 corresponds to the deep-seated scar geometry in Figure 11c, and profile 4 corresponds to the spoon-shaped scar geometry (not shown above).

[43] All the data (images and DTM) have been processed using the Integrated Software for Imagers and Spectrometers (ISIS-3) from USGS [*Torson and Becker*, 1997; *Anderson et al.*, 2004], and integrated in a georeferencing/mapping/digitizing package. ISIS makes it possible to correct data from instrument spice kernels (containing position, velocity and orientation of the satellite and camera regarding to the ground) and to relocate all the data in the same reference frame. Geomorphological analysis was done using a GIS package.

4.2.1. Deposit Identification

[44] Visible imagery is used to distinguish between landslide deposits and the surrounding floor (Figure 8). When visible imagery is not clear enough, infra-red (IR) imagery is used (see also Figure C1 in Appendix C). Actually, IR data retrieves information on surface temperature at day or night. In day time image, the temperature is mainly dependent on the topography and albedo. In contrast, in nighttime data, the temperature largely depends on the thermal inertia of the surface (within the first meter). Therefore, information on nighttime data is mainly dependent on grain size and degree of induration providing indicators of surface properties used here to discriminate landslide deposits from the surrounding floor.

[45] We used here Mars Observer Camera (MOC) images with resolution of 2–5 m/pixel [*Malin and Edgett*, 2000], Thermal Emission Imaging System (THEMIS) visible images (18 m/pixel) and IR images (100 m/pixel) from the Mars Odyssey (MO) probe [*Christensen et al.*, 2003] and High Resolution Stereo Camera (HRSC) images with resolution of 50 m/pixel from Mars Express probe [*Neukum et al.*, 2000] THEMIS data are acquired in five spectral channels for the visible camera (from 0.4 to 0.6 μm) and in ten channels for the IR camera (from 6 to 14 μm).

4.2.2. DTM Reconstruction

[46] Digital Topography Model (DTM) has been reconstructed using the topography data from Mars Observer Laser Altimeter (MOLA) of Mars Global Surveyor (MGS) that provides global altimetric profiles called Precision Experiment Data Records (PEDRs). While interpolated grid are available (gridded at 1/128th of a degree grid, named MEGDR, *Mission Experiment Gridded Data Records*) [*Smith and Zuber*, 1999], with an accuracy of 463 m/pixel in the vicinity of the equator (which is the case for all the studied landslides), we used a kriging method on the PEDR products in order to get a gridded DTM with less artifacts. The High Resolution Stereo Camera (HRSC) onboard Mars Express (MeX) provides DTMs with 125 m/pixel accuracy but were only available for the Ius landslide at the time of this study. HiRISE imagery, providing extracted DTM by stereoscopy with accuracy down to 1 m/pixel locally were not available at the time of the present study. In addition, HiRISE footprints were too small and thus not appropriate for our purpose. DTM extraction from CTX images were also not available at the time of this study.

[47] The reconstruction of the released mass and of the pre-event topography has been performed following a four-step pipeline:

[48] 1. *Deposit removal*. The extent of the deposits, as identified using imagery, is used as a mask in the altimetric grid provided by MOLA. After estimating the thickness of the deposit from the topography data, contour lines are edited, using the digitizing package previously mentioned, and used to manually withdraw the deposit. This method has

Table 2. Volume Calculation of Studied Martian Landslides[a]

	This Study									*Sato et al.* [2007]					
	Spoon-Shape			Deep-Shape			*Quantin et al.* [2004]			Minimum Curvature			Plane Interpolation		
Site	V_i	V_f	ΔV	V_i	V_f	ΔV	V_i	V_f	ΔV	V_i	V_f	ΔV	V_i	V_f	ΔV
Coprates	395	540	+37	**585**[b]	**730**	+25	500	346	−30.69	249	472	+89.44	215	438	+103.5
Ius	2100	2300	+10	**2390**	**2596**	+9	1960	1520	−22.41	–	–	–	–	–	–
Ophir	**740**	**824**	+11	903	1046	+16	9081	5204	−42.69	–	–	–	–	–	–
Ganges	**310**	**530**	+71	340	550	+62	1003	556	−44.52	–	–	–	–	–	–

[a] V_i are initial volumes, V_f are final volumes. $\Delta V = (V_f/V_i - 1) \times 100$ is the balance in percent between V_i and V_f. Note that all ΔV from work by *Quantin et al.* [2004] are negative whereas others are positive.
[b] Boldfacing indicates the volume found with the scar geometry for which the simulation provides the best results compared to observations.

been shown to provide much more realistic and smooth results than any mathematical calculation based on minimization or interpolation of theoretical topographic surface [*Cressie*, 1990]. However the resulting altimetric data does not fit a regular grid. In order to obtain a regular grid without spurious artifacts, a condition required for numerical modeling, the altimetric information has been interpolated with a kriging algorithm [*Cressie*, 1990; *Stein et al.*, 1999]. The kriging method makes it possible to take the spatial position and the spatial variability of the information into account. In our case, this method provided minimal interpolation bias with respect to others classical interpolation methods (e.g., bilinear, bicubic).

[49] 2. *Initial mass reconstruction*. The upper surface of the released mass prior to landsliding can be inferred from the horst morphology on both sides of the landslide scar so as to mimic the wallslopes of each sides of the scar (Figure 9). Then, the second order morphological features shown in Figure 9 are added to the contour lines by extrapolating the spur-and-gully morphology currently observed along the wallslopes that are adjacent to the landslide area (Figure 11b). Thanks to MOLA, spur-and-gully morphology involve roughly 15% of the wallslope's volume.

[50] 3. *Reconstruction of the scar shape*, also obtained by editing the contour lines, is the critical step of the method as constraints on scar geometry are poor due to the deposit cover. The visible upper part of the scar is either gently curved (Ophir and Ganges) or steep (Coprates and Ius). For the first group, the degrees of freedom for reconstruction of the shape of the bottom scar are fewer than for the second group because the curve of the scar can simply be interpolated in the masked areas. Two end-member geometries are considered here: the spoon-seated scar (which mimics the S_1 scar in our 3-D tests in section 3.2 and Figure 3a) and the deep-seated scar (corresponding to the S_3 scar, see section 3.2 and Figure 3c), as shown for example for the Coprates landslide in Figure 11d (profiles 3 and 4, respectively). The geometry of the deep-seated scar is more likely to be planar than curved.

[51] 4. *Refinement of the DTM grid*. The DTM of the pre-slide geometry and of the initial released mass have the same spatial resolution as the initial data grid (e.g., for MOLA spatial resolution is ~463 m/pixel). Note that by comparison, MOLA resolution allows us to describe each landslide with hundreds of points in the runout distance, which is in the same order of magnitude of numerous terrestrial examples [*Kelfoun and Druitt*, 2005; *Pirulli and Mangeney*, 2008; *Sosio et al.*, 2008]. However, landslide modeling requires a finer grid, so artificial refining of the mesh has been performed by interpolating the altimetric grid using the kriging method. Low-pass filtering is performed in order to minimize artificial oscillations in the resulting grid (Figure 11c).

[52] The spatial resolution has been chosen based on simulation of the analytical solution for dam-break granular flows developed by *Mangeney et al.* [2000], with characteristic dimensions of the granular dam similar to those of Martian landslides. The second order numerical scheme implemented in SHALTOP has made possible a space step dx = 130 m over a grid of typically 1100 × 1100 points, which accurately reproduces the resolution of the analytical solution. This spatial resolution was obtained with the MOLA DTM; for the Ius Chasma landslide, where the HRSC-derived DTM is available, dx = 80 m, could be obtained.

[53] For volume calculation (initial and final mass of the landslide), the Simpson's rule for numerical integration was used for a better accurate results in numerical integration compared to simple numerical integration (see *Press et al.* [1988] for further details).

4.3. Frictional Properties of Martian Landslides

[54] As it has been shown previously in the theoretical tests, the runout distance is a very robust parameter that is only poorly affected by the uncertainty on scar geometry. For this reason, the friction angles δ retained here are the ones for which the observed runout distances are reached numerically. The resulting values of the fitted friction angles δ obtained using Coulomb friction law for the four landslides are displayed in Table 2. The calibrated friction angle ranges in $\delta \in [7.2°, 9.8°]$, i.e., $\delta = 8.5° \pm 1.3°$ for the landslides investigated here. As a result, the friction coefficient is almost the same for all considered landslides. Furthermore the normalized runout as a function of the initial aspect ratio for each considered landslide lies on a similar trend also suggesting a common friction coefficient (Figure 12).

[55] These simulations show that, the friction coefficients required to reproduce the long distances traveled by Martian landslides are much smaller than those expected for granular flows (~30°). Such small friction coefficients for natural landslides compared to granular flows in laboratory have been reported for most terrestrial events [e.g., *Pirulli and Mangeney*, 2008; *Kuo et al.*, 2009]. However, the difference in geological context as well as in the material involved between two terrestrial landslides made it difficult to assess

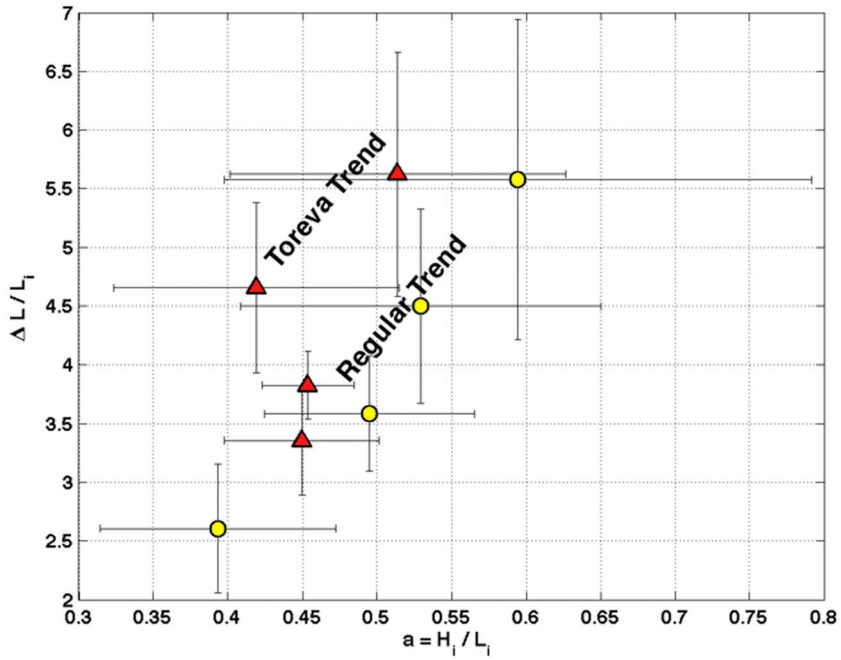

Figure 12. Normalized runout as a function of the initial aspect ratio ($a = H_i/L_i$) for some large Martian landslides (see Table 1). Red triangles are landslides simulated in this study. The two landslides with a shifted trend are Coprates and Ganges landslides, which both have Toreva blocks.

the relevance of the friction coefficient as an indicator of the mean frictional dissipation during the flow, independently of the initial geometry and volume of the released mass.

[56] Only single-event landslides have been considered here (e.g., one event per scar is assumed), although multievent process has been proposed by former studies [*Quantin et al.*, 2004; *Bulmer and Zimmerman*, 2005]. More than fifty examples are observed on Mars. Some of them a clearly multievents as they show overlap deposits. For some others, the question might be still open and subject of debate. Multiple events result in superimposed debris aprons whose cross-cutting show upwell in both topography and morphology, for instance in eastern Ius Chasma. Debris apron superimposition is not observed in the studied cases, for example, Coprates clearly shows a single arrowhead apron indicative of a single event (see Figure 8). Because multievent case might have some effect on the friction angle needed in numerical simulations, multievent have been simulated by first releasing half of the mass, then releasing the second half once the first half stopped. It came out that (1) the observed deposits shape was not reproduced and (2) smaller friction angle is required in order to reach the observed runout. For example, Coprates needs a friction angle below 4.5°, which is roughly two times smaller than the value needed in the case of a single event.

[57] As a result, in any circumstance (e.g., single or multi event), Martian landslides show a very low dissipation compared to dry sand media. According to our results, a recent study based on discrete element modeling shown that reproducing the runout of another Martian landslide (also observed in Ganges Chasma) needs a null basal friction angle and an internal friction angle equal to 5° [*Smart et al.*, 2010].

[58] Such a small value of the dissipation in natural landslides is still largely debated and could result from various physical processes such as fluid content, fluidization, fracturing, granulometry, and perhaps other processes such as air cushioning, erosion effects, acoustic fluidization, and floor vibration induced by the mass spreading [e.g., *Barkan*, 1962; *Melosh*, 1979; *Hungr and Evans*, 2004; *Davies and McSaveney*, 1999; *Buss and Heim*, 1881; *Sassa*, 1985; *Legros*, 2002; *Sassa*, 1988; *Abele*, 1997; *Roche et al.*, 2004, 2011; *Mangeney et al.*, 2007b, 2010; *Mangeney*, 2011].

[59] Another explanation could be the presence of a weaker material at the base of the massif as previously proposed by *Bigot-Cormier and Montgomery* [2007]. Friction angles calculated in this study from maximum stable relief (based on the Culmann wedge model which is intensively used in geomorphological studies to empirically constrain the maximum unfailed height) are in a good agreement with those needed in the present simulations ($8° < \delta < 10°$). Moreover, this model could also explain the presence of Toreva blocks for Ganges and Coprates cases since such landslides are observed on Earth when "[…] a single large mass of unjostled material which, during descent, has undergone a backward rotation toward the parent cliff about horizontal axis […] such blocks have developed from cliffed sections of low-dipping strata in which one or more relatively coherent beds rest upon others which are either incoherent or capable of so becoming when wetted." [*Reiche*, 1937]. Detailed analysis of the landslide initiation process however requires using models able to deal with the complex evolution toward destabilization due to external forcing or material damaging [see, e.g., *Deboeuf et al.*, 2005].

[60] In addition, Coprates and Ganges cases need lower friction angle (see Table 1) and present also greater runout than other studied landslides. However, evidence for such weak materials is not obvious in Valles Marineris.

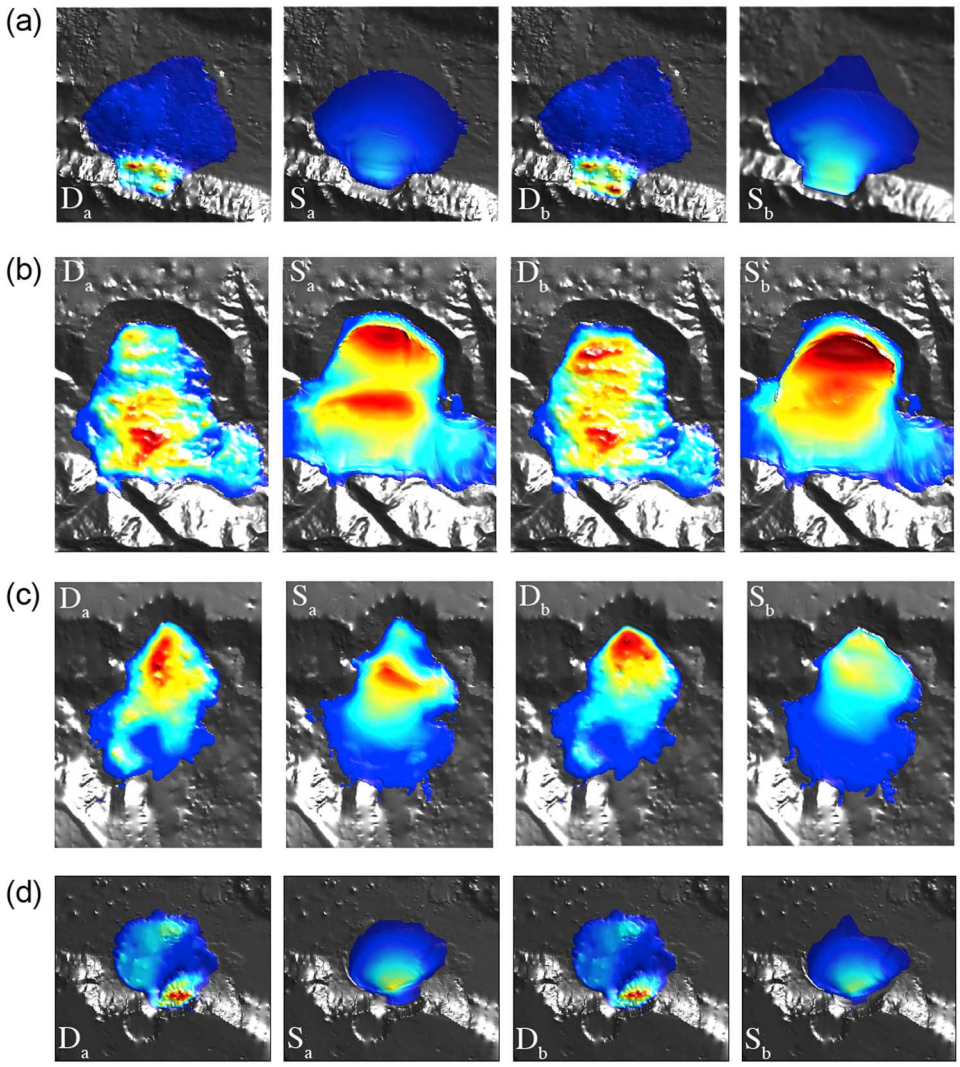

Figure 13. Comparison between observations (D_i) and numerical simulations (S_i) using two end-member topographies (spoon-seated type scar geometry for $i = a$ and deep-seated type scar geometry for $i = b$) for (a) Coprates Chasma, (b) Ius Chasma, (c) Ophir Chasma and (d) Ganges Chasma landslides. (See Figures 3a–3c as reference for scar geometry.)

4.4. Simulated Deposit and Scar Geometry

[61] As done in the theoretical tests, different morphologies of the initial scar (two for each landslide) are tested here to assess their effects on the simulated landslide deposit. Martian topography data provide constraints on the upper part of the scar geometry (e.g., the final deposit does not necessarily fully cover the scar). As a result, the degree of freedom for reconstructing the scar geometry are fewer for natural examples than for the theorical 3-D tests studied in section 3.2. Furthermore, the range of possible geometries varies from one example to another.

[62] As shown in Figures 13a and 13b, deep-seated geometries gives better results for both Coprates and Ius landslides.

[63] Ophir Chasma gives a very small degrees of freedom for scar geometry reconstruction due to the outcropping part of the failure. Only smoothed-scar type reconstructed geometries can match the upper visible part of the scar. For this reason, both geometries give very similar simulated shapes of the deposit (Figure 13c). In both cases, the runout distance, the 3-D shape of the deposit and the overall mass distribution matches the observations well.

[64] Ganges Chasma provides limited constraints on the initial wallslope, because of the post-landslide back-wasting of the scar wall relative to that of other landslides in this study (Figure 8d). The spoon-seated geometry results in a fan-shaped deposit, in good agreement with observations, and in contrast to arrow-shaped deposit that results from deepest-scar at Coprates Chasma (Figure 13d).

[65] The difference in the simulated deposit shape obtained for different scar geometry is easier to observe for Coprates and Ganges landslides that were not affected during the flow by any obstacles or underlying previous deposits.

4.5. Volume Balance

[66] The volume of the initial released mass V_i and the volume of the deposit V_f including the Toreva block and

debris aprons have been calculated for each landslide using the reconstructed DTM. Volume calculations are performed for the both scar geometries (Table 2).

[67] Volume estimates of Coprates landslide have been previously calculated by *Quantin et al.* [2004] using linear interpolation between the edges of the scar and by *Sato et al.* [2007] through manual identification of the deposits followed by automatic interpolation using both bilinear and minimum curvature algorithms (see Table 2). These formers studies used the gridded data derived from MOLA shots (MEGDR) because this is more convenient. However, the grid provides interpolation of raw MOLA data points separated by huge areas where the topography is unknown, especially around the equator. Consequently, using the MOLA grid instead of the raw MOLA data points may lead major artifacts in the topography that are likely to affect the simulation results (a comparison between several interpolation algorithms from the PEDR products is provided in the auxiliary material).[1]

[68] For both the smooth and deep-seated scar geometry, the calculated final volume is similar to the volume found by *Quantin et al.* [2004] but is about the double of the values obtained by *Sato et al.* [2007], probably in part because they did not take the Toreva block in the volume calculation into account. Furthermore, the DTM reconstruction procedure developed here does not produce the spurious oscillations that are observed in the DTM calculated by *Sato et al.* [2007]. These oscillations may generate minor errors in volume calculation as well.

[69] More importantly, the volume balance $\Delta V = V_f - V_i$ between the initial mass and the final deposit calculated here is positive, ranging from ΔV = 9% ± 10% for the Ius landslide to ΔV = 71% ± 10% for Ganges landslide. Examples with Toreva show a greater ΔV suggesting either less accuracy in reconstruction or a greater dilatancy in the flowing part of the deposit. Increase in volume from the initial to the final state is also reported by *Sato et al.* [2007] for the Coprates landslide, whereas negative volume change has been calculated by *Quantin et al.* [2004] (see Table 2). As this supposed decrease in volume has been interpreted as thermokarst by *Quantin et al.* [2004], our calculation suggest, on the contrary, a dilation of the granular mass and/or presence of loose material on the canyon floor incorporated into the landslide. Such dilation is classically observed for terrestrial landslides as a result of rock fragmentation. *Hungr* [1981] reports typical values of volume increase ranging from 7%–40% close to the range of the volume change calculated here for Valles Marineris landslides. Similar values have also been measured experimentally on well-sorted crushed rock samples [*Sherard et al.*, 1963].

4.6. Landslide Seating Implications and Geological Context

[70] Numerical simulations suggests that despite an apparently similar geological context, i.e., the Valles Marineris rift, landsliding may have developed different scar geometries that could be related to different fault distributions and possibly different triggering mechanisms.

[71] As discussed in the previous section, the shapes of the deposits of the Coprates and Ius Chasma landslides are better reproduced if a deep-seated geometry of the initial scar is assumed whereas Ophir and Ganges are better reproduced using a spoon-seated scar geometry. Deep-seated and spoon-seated geometries may result from different triggering and failure mechanisms.

[72] Deep-seated scar may result from gravitational slip along pre-existing faults dipping 50–60°, typically normal faults, while spoon-shaped scars are less steep and less likely to reactivate normal faults [*Mège and Bourgeois*, 2010].

[73] In Coprates Chasma landsliding from reactivation of a normal fault is supported by evidence of scar development along an uphill-facing normal fault scarp near the top of the Coprates ridge. It may be speculated that seismic shaking along one of the uphill-facing faults located along the southern Coprates horst wall triggered the landslide, removing more than half the ridge topographic relief and generating fast-moving flow. The simulations performed here suggest maximum velocities in the order of ~100 $m.s^{-1}$, which is in agreement with observations in Figure 9. This scenario challenges an alternative interpretation of the Ganges landslide as a slow moving mass resulting from gravitational failure over millions of years [*Bulmer and Zimmerman*, 2005].

[74] The range of scar geometries inferred from this study reflects a distinction that can be made between chasmata whose formation resulted from regional, crustal-scale extension by brittle tectonics, and chasmata in which the structural control is much weaker [see *Peulvast et al.*, 2001]. The latter likely initiated as basins without any observable significant help from brittle tectonics, perhaps as large-scale collapse features [*Adams et al.*, 2009] sometimes called ancestral basins [*Schultz*, 1998]. Ius and Coprates chasmata are tectonics-dominated chasmata [*Schultz*, 1991, 1995; *Peulvast and Masson*, 1993; *Mège and Masson*, 1996; *Peulvast et al.*, 2001], whereas Ganges and Ophir chasma are typical examples of ancestral basins. This could explain the steep Ius and Coprates chasma landslide scar, controlled by regional normal faulting, and the gentle Ganges and Ophir sliding planes, less influenced by earlier brittle tectonic structures.

5. Conclusions

[75] Numerical simulation of theoretical granular flows and of real Martian landslides has been performed to assess the influence of the initial scar geometry on the landslide deposit and on the calculation of the released volume. Satellite data have been processed to construct Digital Topography Models used as inputs in granular flow modeling. Different initial scar geometries have been tested in both theoretical and real landslide simulations ranging from rounded conic shape to steep wall geometry.

[76] Numerical modeling shows that the runout distance is a very robust parameter that is only weakly influenced by the geometry of the initial scar. The errors in the definition of the scar geometry will generate an error of ~1° on the friction angle obtained by back-analysis of the runout distance, justifying its extensive use to describe natural landslide dynamics and to calibrate numerical models. The thickness profile of the deposit in the main flow direction is also not very sensitive to the initial shape of the scar. On the

[1] Auxiliary materials are available in the HTML. doi:10.1029/2011JE003803.

contrary, the scar geometry strongly affects the lateral spreading and the overall shape of the deposit. Scars involving gentle conic lateral walls lead to rounded fan-shaped deposits whereas scars involving steep lateral walls generate arrow-shape deposits. As a result, information on the shape of the initial scar, generally unknown in field application, can be recovered from the observation of the landslide deposit shape, provided that the flow is not confined by the surrounding topography. The increasing precision on scar geometries provided by our study should help constrain geomechanical models designed to deduce information on the material properties from the geometry of the failure zone. Such constraints on scar geometry can, with the aid of slope stability analyses, be used to constrain the destabilization processes and provide insight into the mechanical properties of the material involved, with significant implications for risk assessment. A second study will focus on the transition between static body to the spreading phase using geotechnical tools.

[77] Furthermore, by providing information on the geometry of the scar, the observation of the shape of the deposit can help constrain the initial volume involved in landsliding, a major ingredient in mass balance calculation, rather than relying on the estimated final deposits volume calculation as usually used for Martian landslides. All these results suggest a simple procedure for landslide numerical modeling: (1) infer information on scar geometry and initial released mass from deposit shape, (2) fit the friction coefficient to the runout distance.

[78] Surprisingly, Martian landslide deposits in Valles Marineris exhibit the same shapes as the simulated deposits obtained by varying the geometry of the initial scar (at least when the deposits are not affected by any obstacle, as for Coprates and Ganges landslides). While the deposit shape of the Coprates and Ius landslides indicate a deep-seated initial scar with steep slopes, implying a fault-controlled triggering mechanism, Ophir and Ganges Chasma landslides are better reproduced using a spoon-shaped, rounded initial scar, for which structural control is likely weaker or absent.

[79] Geological observations support these interpretations, since Ius and Candor chasmata are primarily horst-and-graben features whereas Ophir and Ganges chasmata are primarily ovoid basin features in which brittle structural control is weak. The surprising agreement between failure characteristics deduced from deposit extent and the local geological context shows that numerical modeling coupled with analysis of deposit extent helps retrieve information on the failure conditions.

[80] The more accurate volume calculation performed here suggests that whatever the uncertainty on the initial scar geometry, the volume of the deposit of Martian landslides is greater than the initial released volume. This challenges the previous conclusion of *Quantin et al.* [2004] that there was a decrease of volume between the initial and final state. The increase in volume calculated here and assumed to be related to dilatancy effects, is in the range of the volume increase measured on terrestrial landslides (ΔV = 10–40%) [*Hungr and Evans*, 2004].

[81] Best fit of the observed runout distance has been obtained using almost the same friction angle $\delta = 8.5° \pm 1.3°$ whatever the considered landslide. As a result, the friction coefficient provides a measure of the empirical friction during landslide flow, independent of the released mass and the underlying topography. The small value of the friction angle compared to the friction angle typical of granular material suggests a smaller dissipation than that observed for dry granular flows in the laboratory that are well reproduced using numerical modeling with friction coefficient ranging from 25° to 35° [e.g., *Iverson et al.*, 2004; *Mangeney-Castelnau et al.*, 2005; *Mangeney et al.*, 2007a, 2007b; *Pudasaini and Hutter*, 2007]. The observed small dissipation in natural landslides is often reported in the literature but its interpretation in terms of physical processes during emplacement is still an open issue.

Appendix A: The SHALTOP Model

[82] Contrary to classical approaches, the thin layer model SHALTOP is written in a fixed cartesian reference frame with the shallowness approximation imposed in the direction perpendicular to the topography [see *Bouchut et al.*, 2003; *Bouchut and Westdickenberg*, 2004; *Mangeney-Castelnau et al.*, 2005; *Mangeney et al.*, 2007a]. More specifically, the equations are derived in a horizontal/vertical fixed reference frame (x, y, z), as opposed to the equations developed by Hutter and co-workers in a variable reference frame linked to the topography (X, Y, Z). However, the shallowness assumption is still imposed in the local reference frame (X, Y, Z). Indeed, to satisfy the hydrostatic assumption for shallow flow over inclined topography, it is the acceleration normal to the topography that must be neglected compared to the gradient of the pressure normal to the topography. The rigorous asymptotic analysis makes it possible for the first time to account for the whole curvature tensor of the topography defined by

$$\mathcal{H} = c^3 \begin{pmatrix} \dfrac{\partial^2 b}{\partial x^2} & \dfrac{\partial^2 b}{\partial x \partial y} \\ \dfrac{\partial^2 b}{\partial x \partial y} & \dfrac{\partial^2 b}{\partial^2 b} \end{pmatrix}, \tag{A1}$$

where the scalar function $b(x, y)$ describes the 3-D topography. The 2-D horizontal coordinate vector is $\mathbf{x} = (x, y) \in \mathrm{R}^2$ and the 3-D unit upward normal vector is

$$\vec{n} \equiv (-\mathbf{s}, c) \in \mathrm{R}^2 \times \mathrm{R}, \quad \text{with} \quad \mathbf{s} = \frac{\nabla_{\mathbf{x}} b}{\sqrt{1+\|\nabla_{\mathbf{x}} b\|^2}}, \quad \text{and} \quad c = \frac{1}{\sqrt{1+\|\nabla_{\mathbf{x}} b\|^2}}, \tag{A2}$$

where $\nabla_{\mathbf{x}}$ is the gradient of the topography in the horizontal plane, and $c = \cos\theta$, with θ the angle between $\vec{n}$ and the vertical direction. Here the 3-D vectors are represented using an arrow $\vec{\cdot}$ and the 2-D vectors using bold letters. The flow is described by

$$h(t,x) \geq 0, \qquad u'(t,x) \in R^2 \tag{A3}$$

where h is the thickness of the material layer in the direction normal to the topography, and $\mathbf{u}' = (u, u_t)$ (where the subscript t stands for *transverse*) is a parametrization of the velocity. The real 3-D material velocity has horizontal/vertical components

$$\vec{\mathbf{u}} = (c\mathbf{u}', \mathbf{s} \cdot \mathbf{u}'). \tag{A4}$$

This physical velocity is tangent to the topography, $\vec{\mathbf{u}} \cdot \vec{n} = 0$, and can be expressed as a 2-D vector $\mathbf{u} = (u, v)$ in the

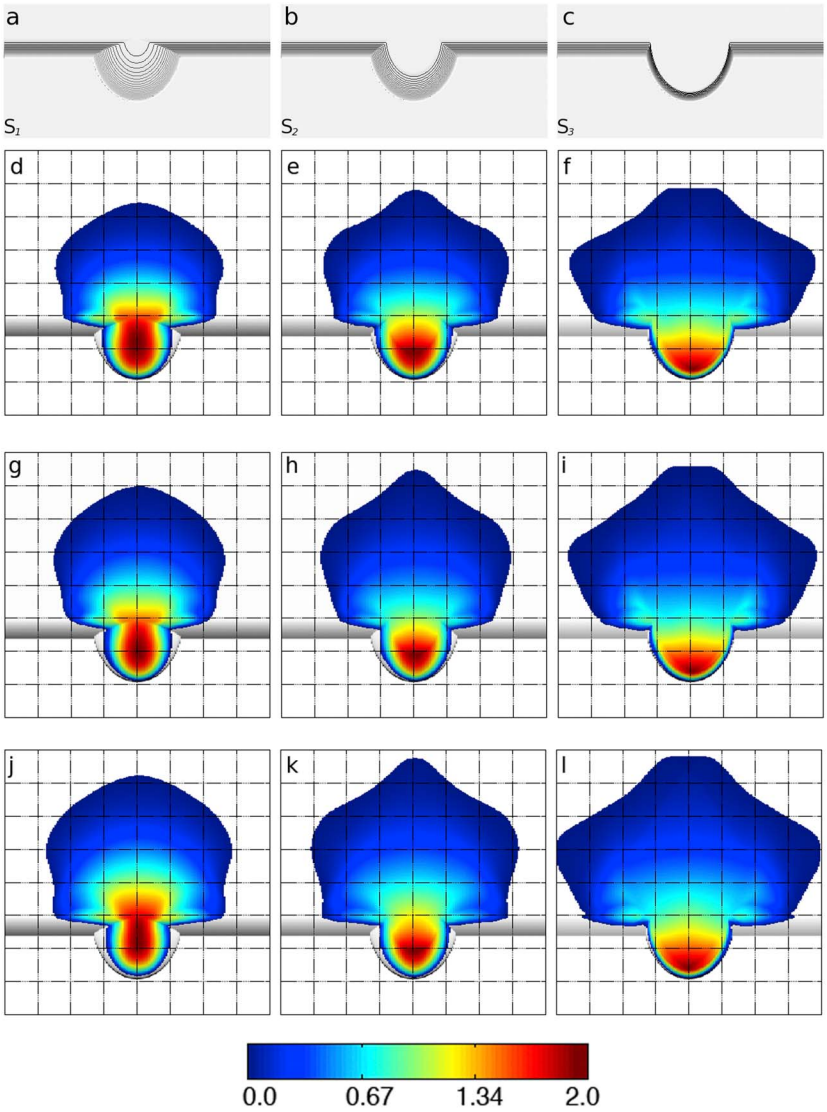

Figure B1. 3-D simulations complements. (a–c) Shaded relief of the 3 geometries S_i, $i \in [1, 3]$. (d–f) Deposits of simulated landslides for each S_i over flat floor ($\theta = 0°$ in equation (2)) using $\delta = 12°$. (g–i) Deposits over inclined floor ($\theta = 2°$) using $\delta = 12°$. (j–l) Deposits over flat floor using $\delta = 10°$.

(X, Y) plane. In 1-D, $\mathbf{u}'$ is actually the real scalar velocity u in the plane tangent to the topography. For flow over an inclined plane with slope in the x-direction, the real physical velocity has coordinates in the (X, Y) plane given by $\mathbf{u} = (u, v) = (u, cu_t)$.

[83] In the horizontal Cartesian coordinate formulation, the model can be expressed as

$$\partial_t(h/c) + \nabla_{\mathbf{x}} \cdot (h\mathbf{u}') = 0, \tag{A5}$$

$$\partial_t \mathbf{u}' + c\mathbf{u}' \cdot \nabla_{\mathbf{x}} \mathbf{u}' + \frac{1}{c}(Id - ss^t)\nabla_{\mathbf{x}}(g(hc + b)) = -\frac{1}{c}(\mathbf{u}''\mathcal{H}\mathbf{u}')\mathbf{s} + \frac{1}{c}(\mathbf{s}^t\mathcal{H}\mathbf{u}')\mathbf{u}' - \frac{g\mu c\mathbf{u}'}{\sqrt{c^2\,\|\mathbf{u}'\|^2 + (\mathbf{s}\cdot\mathbf{u}')^2}}\left(1 + \frac{\mathbf{u}''\mathcal{H}\mathbf{u}'}{gc}\right)_+ \tag{A6}$$

where $\nabla_{\mathbf{x}}$ is the gradient vector in the horizontal x, y plane and g acceleration due to gravity. The subscript + stands for the positive part, $x_+ = \max(0, x)$.

[84] For flow over an inclined plane, the equations reduce to

$$\frac{\partial h}{\partial t} + c\frac{\partial (hu)}{\partial x} + \frac{\partial (hv)}{\partial y} = 0, \tag{A7}$$

$$\frac{\partial u}{\partial t} + cu\frac{\partial u}{\partial x} + v\frac{\partial u}{\partial y} + c\frac{\partial (ghc)}{\partial x} = -g\sin\theta + f_x, \tag{A8}$$

$$\frac{\partial v}{\partial t} + cu\frac{\partial v}{\partial x} + v\frac{\partial v}{\partial y} + \frac{\partial (ghc)}{\partial y} = f_y \tag{A9}$$

where $\mathbf{f} = (f_x, f_y)$ is the friction force parallel to the inclined plane. Note that introducing the coordinate X in the inclined

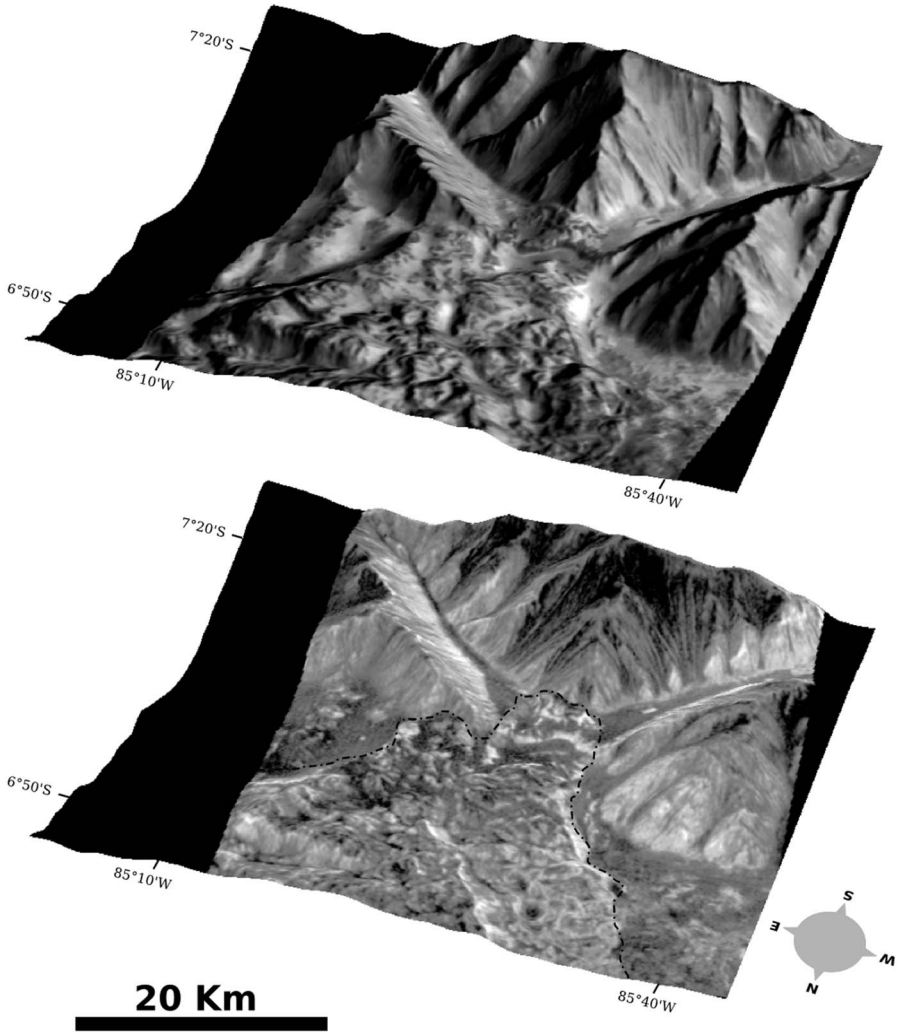

Figure C1. Identification of the deposit using thermal inertia on IR THEMIS data. (top) Daytime and (bottom) nighttime THEMIS IR images draped on HRSC DTM for Ius landslide deposits. The strong difference between the reflectance of the landslide deposit and of the surrounding floor makes it easier to define the deposit outline than on visible images.

direction instead of x, i.e., $X = x/c$, gives $c\partial/\partial x = \partial/\partial X$, and (9)–(11) can then be reduced to the classical Savage and Hutter equations. The transition between a static state ($\mathbf{u} = 0$) and a flowing state, typical of granular material, is modeled by introducing a Coulomb threshold σ_c. The motion is allowed only if the norm of the driving forces $\|\mathbf{f}\|$ exceeds the Coulomb threshold [*Mangeney-Castelnau et al.*, 2003]. In the model (10)–(11), $\mathbf{f}$ is expressed as

$$\begin{aligned} \| \mathbf{f} \| \geq \sigma_c \quad &\Rightarrow \quad \mathbf{f} = -gc\mu \frac{\mathbf{u}}{\| \mathbf{u} \|}, \\ \| \mathbf{f} \| < \sigma_c \quad &\Rightarrow \quad \mathbf{u} = \mathbf{0}, \end{aligned} \tag{A10}$$

where $\sigma_c = gc\mu$, where $\mu = \tan\delta$ is the friction coefficient, δ being the friction angle. When the material exceeds the Coulomb threshold, the Coulomb friction law states that when flowing, the friction force has a direction opposite to the averaged tangential velocity field and the amplitude of the friction force is governed by the total overall pressure and the friction coefficient μ. h and the Froude number of the flow $Fr = \|\mathbf{u}\|/\sqrt{gh}$, where $\|\mathbf{u}\|$ stands for the flow velocity, hereafter called Pouliquen flow rule [*Pouliquen and Forterre*, 2002]:

if $Fr > \beta$

$$\mu(h, Fr) = \tan\delta_1 + (\tan\delta_2 - \tan\delta_1)\frac{1}{\frac{\beta h}{FrL} + 1}. \tag{A11}$$

if $Fr = 0$

$$\mu(h, Fr) = \tan\delta_3 + (\tan\delta_4 - \tan\delta_3)\frac{1}{\frac{h}{L} + 1}. \tag{A12}$$

where δ_i, $i = 1, 4$ are characteristic friction angles of the material, L is a lengthscale that can be deduced from laboratory measurements and $\beta = 0.136$ is a dimensionless parameter. An empirical fit between the two expressions is

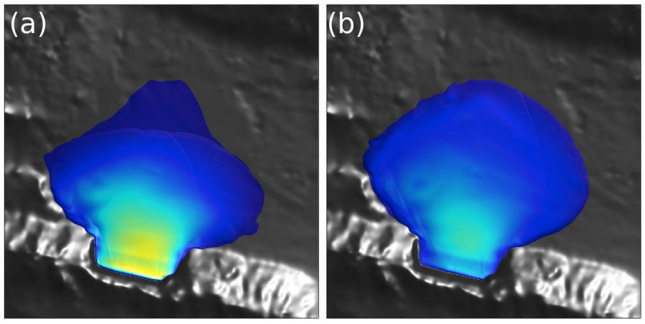

Figure D1. Comparison between (a) Coulomb and (b) Pouliquen friction laws for Coprates landslide using $\delta_{i=1,4} = 5°$, 15°, 7°, 17° and $L = 1$. The Pouliquen's law produces the correct runout, but does not replicate deposit shape.

used for $0 \leq Fr \leq \beta$. More details on this flow law are given by *Pouliquen and Forterre* [2002] and by *Mangeney et al.* [2007a] (section 3.2). Basically, in Pouliquen flow rule, the friction coefficient increases when the thickness h decreases and the velocity u increases.

[85] As the Pouliquen flow rule has been successful in reproducing experimental granular flows and some natural landslides [e.g., *Pouliquen and Forterre*, 2002; *Mangeney et al.*, 2007a; *Pirulli and Mangeney*, 2008; *Mangold et al.*, 2010], its use in modeling of natural flows is difficult because of the high number of involved parameters. In contrast, the Coulomb friction law only involves one empirical parameter, the friction angle δ.

[86] The numerical scheme is based on the work of *Bouchut* [2004] and is detailed by *Mangeney-Castelnau et al.* [2005] and *Mangeney et al.* [2007a]. It is a second order scheme that preserves the steady states as well as other requirements related to the resolution of hyperbolic equations. Recently, this code has been enhanced into MPI version allowing the user to perform a simulation with a huge space resolution. Taking advantage of computing facilities of IPGP, this new version SHALTOP^{MPI} is able to simulate large Martian landslides (more than 1.10^6 grid nodes are used in the simulations).

Appendix B: 3-D Simulation Complements

[87] As described in section 3.2, unconfined tests have been performed dealing with (1) the scar geometry, (2) the friction angle and (3) the slope of the bottom topography. In agreement with equation (2), increasing the slope will result similarly than decreasing the friction angle, especially for small slope and friction angles (Figure B1). Both shape and runout distance simulated with $\theta = 2°$ and $\delta = 12°$ are similar to those obtained with $\theta = 0°$ and $\delta = 10°$. Nevertheless, lateral spreading is wider for this last group of simulations.

Appendix C: Identification of the Deposit Using Thermal Inertia on IR THEMIS Data

[88] As thermal inertia is linked to induration of material, THEMIS-IR data at night can be used to identify landslide deposits which are less indurated that surrounding floor of Valles Marineris Chasma (Figure C1). We used the THEMIS IR data set when daytime visible imagery were not sufficient for deposits identification.

Appendix D: Simulation Complements

[89] Simulations using the Pouliquen flow rule (see section 2) have also been performed to investigate the effect of the friction law in the results. Because a systematic calibration of all the parameters involved in the Pouliquen flow rule would have been too long for the specific purpose of this paper, we only simulated the Coprates landslides as this example presented an interesting challenge. Pouliquen law (here dealing with $\delta_1 = 5°$, $\delta_1 = 15°$, $\delta_3 = 7°$, $\delta_4 = 17°$ and $L = 1$.) seems to be able to catch the shape of the deposits as shown in Figure D1. This reason is linked to the fact that the friction increases when the thickness h decreases (see equations (A11)–(A12)). As the arrow area concerns the thinner and the fastest part, the friction is greater very important in this region of the flow.

[90] **Acknowledgments.** The authors would like to thank P. Stoclet for his work on the parallelization of the model, which resulted in a substantial enhancement of grid resolution and time gain, and the Planetary Data Server for the availability of the Martian data online,G. Neumann and C. H. Acton for helpful support in using MOLA and kernel data, and finally Randolph Kirk and Trent Hare from Astrogeology Branch Team of the USGS for very helpful technical support in ISIS use. This work benefitted from fruitful discussions with O. Hungr and J-.P. Peulvast as well as previous review of K. Harrison as well as O. Barnouin and other anonymous reviewers for their helpful comments. Authors would also thank A. Limaye and N. Cubas for English corrections and improvements of the text. This study has benefitted from the Service de Calcul Parallèle et de Traitement de Données en sciences de la Terre (S-CAPAD) of IPGP. This work has been supported by ANR PLANETEROS, IPGP contribution 3174.

References

Abele, G. (1997), Rockslide movement supported by the mobilization of groundwater-saturated valley floor sediments, *Z. Geomorphol.*, *41*, 1–20.

Adams, J. B., A. R. Gillespie, M. P. A. Jackson, D. R. Montgomery, T. P. Dooley, J.-P. Combe, and B. C. Schreiber (2009), Salt tectonics and collapse of Hebes Chasma, Valles Marineris, Mars, *Geology*, *37*, 691–694.

Anderson, J. A., S. C. Sides, D. L. Soltesz, T. L Sucharski, and K. J. Becker (2004), Modernization of the integrated software for imagers and spectrometers, *Lunar Planet. Sci.*, *XXXV*, Abstract 2039.

Barkan, D. D. (1962), *Dynamics of Bases and Foundations: Rock Mass and Mud Wave Deposit*, translated by L. Drashevska, 434 pp., McGraw-Hill, New York.

Bigot-Cormier, F., and D. R. Montgomery (2007), Valles Marineris landslides: Evidence for a strength limit to Martian relief?, *Earth Planet. Sci. Lett.*, *260*, 179–186.

Bouchut, F. (2004), *Nonlinear Stability of Finite Volume Methods for Hyperbolic Conservation Laws, and Well-Balanced Schemes for Sources*, *Front. Math. Ser.*, 134 pp., Birkhäuser, Boston, Mass.

Bouchut, F., and M. Westdickenberg (2004), Gravity driven shallow water models for arbitrary topography, *Commun. Math. Sci.*, *2*, 359–389.

Bouchut, F., A. Mangeney-Castelnau, B. Perthame, and J. P. Vilotte (2003), A new model of Saint-Venant and Savage-Hutter type for gravity driven shallow water flows, *C. R. Math.*, *336*, 531–536.

Bulmer, M. H., and B. A. Zimmerman (2005), Reassessing landslide deformation in Ganges Chasma, Mars, *Geophys. Res. Lett.*, *32*, L06201, doi:10.1029/2004GL022021.

Buss, E., and A. Heim (1881), *Der Bergsturz von Elm*, 133 pp., Worster, Zurich, Switzerland.

Christensen, P. R., et al. (2003), Morphology and composition of the surface of Mars: Mars Odyssey THEMIS results, *Science*, *300*, 2056–2061.

Cressie, N. A. C. (1990), The origins of kriging, *Math. Geol.*, *22*, 239–252.

Cruden, D. M., and O. Hungr (1986), The debris of the Frank Slide and theories of rockslide-avalanche mobility, *Can. J. Earth Sci.*, *23*, 425–432.

Cruden, D. M., and D. J. Varnes (1996), Landslide types and processes, in *Landslides: Investigation and Mitigation*, edited by A. K. Turner and R. L. Shuster, *Spec. Rep. 247*, pp. 36–75, Transp. Res. Board, Washington, D. C.

Dade, W. B., and H. E. Huppert (1998), Long-runout rockfalls, *Geology*, *26*, 803–806.

Davies, T. R. H., and M. J. McSaveney (1999), Runout of dry granular avalanches, *Can. Geotech. J.*, *36*, 313–320.
Deboeuf, S., O. Dauchot, L. Staron, A. Mangeney, and J. P. Vilotte (2005), Memory of the unjamming transition during cyclic tiltings of a granular pile, *Phys. Rev. E*, *72*, 051305.
Denlinger, R. P., and R. M. Iverson (2001), Flow of variably fluidized granular masses across three-dimensional terrain: 2. Numerical predictions and experimental tests, *J. Geophys. Res.*, *106*, 553–566.
Denlinger, R. P., and R. M. Iverson (2004), Granular avalanches across irregular three dimensional terrain: 1. Theory and computation, *J. Geophys. Res.*, *109*, F01014, doi:10.1029/2003JF000085.
Favreau, P., A. Mangeney, A. Lucas, G. Crosta, and F. Bouchut (2010), Numerical modeling of landquakes, *Geophys. Res. Lett.*, *37*, L15305, doi:10.1029/2010GL043512.
Félix, G., and N. Thomas (2004), Relation between dry granular flow regimes and morphology of the deposits: Formation of levees in pyroclastic deposits, *Earth Planet. Sci. Lett.*, *221*, 197–231.
Harrison, K. P., and R. E. Grimm (2003), Rheological constraints on Martian landslides, *Icarus*, *163*, 347–362.
Hogg, A. J. (2008), Two dimensional granular slumps down slopes, *Phys. Fluids*, *19*, 093301.
Hungr, O. (1981), Dynamics of rock avalanches and other types of mass movements, Ph.D. thesis, 500 pp., Univ. of Alberta, Edmonton, Canada.
Hungr, O. (1995), A model for the runout analysis of rapid flow slides, debris flows, and avalanches, *Can. Geotech. J.*, *32*, 610–623.
Hungr, O. (2008), Simplified models of spreading flow of dry granular material, *Can. Geotech. J.*, *45*, 1156–1168.
Hungr, O., and S. G. Evans (2004), Entrainment of debris in rock avalanches: An analysis of a long run-out mechanism, *Geol. Soc. Am. Bull.*, *116*, 1240–1252.
Iverson, R. M. (1997), The physics of debris flows, *Rev. Geophys.*, *35*, 245–296.
Iverson, R. M., M. Logan, and R. P. Denlinger, (2004), Granular avalanches across irregular three-dimensional terrain: 2. Experimental tests, *J. Geophys. Res.*, *109*, F01015, doi:10.1029/2003JF000084.
Kelfoun, K., and T. H. Druitt (2005), Numerical modeling of the emplacement of Socompa rock avalanche, Chile, *J. Geophys. Res.*, *110*, B12202, doi:10.1029/2005JB003758.
Kerswell, R.R. (2005), Dam break with Coulomb friction: A model for granular slumping?, *Phys. Fluids*, *17*, 057101.
Kuo, C. Y., Y. C. Tai, F. Bouchut, A. Mangeney, M. Pelanti, R. F. Chen, and K. J. Chang (2009), Simulation of Tsaoling landslide, Taiwan, based on Saint Venant equations over general topography, *Eng. Geol. Amsterdam*, *104*, 181–189.
Lacaze, L., J. C. Phillips, and R. R. Kerswell (2008), Planar collapse of a granular column: Experiments and discrete element simulations, *Phys. Fluids*, *20*, 063302.
Lajeunesse, E., A. Mangeney-Castelnau, and J.-P. Vilotte (2004), Spreading of a granular mass on an horizontal plane, *Phys. Fluids*, *16*, 2371–2381.
Lajeunesse, E., C. Quantin, P. Allemand, and C. Delacourt (2006), New insights on the runout of large landslides in the Valles-Marineris canyons, Mars, *Geophys. Res. Lett.*, *33*, L04403, doi:10.1029/2005GL025168.
Legros, F. (2002), The mobility of long runout landslides, *Eng. Geol. Amsterdam*, *63*, 301–331.
Lube, G., H. E. Huppert, R. S. J. Sparks, and M. A. Hallworth (2004), Axisymmetric collapses of granular columns, *J. Fluid Mech.*, *508*, 175–199.
Lucas, A., and A. Mangeney (2007), Mobility and topographic effects for large Valles Marineris landslides on Mars, *Geophys. Res. Lett.*, *34*, L10201, doi:10.1029/2007GL029835.
Lucas, A., A. Mangeney, F. Bouchut, M. O. Bristeau, and D. Mège (2007) Benchmark excercises for granular flows, paper presented at 2007 International Forum on Landslide Disaster Management, Hong Kong Geotech. Soc., Hong Kong.
Lucas, A., A. Mangeney, D. Mège, and K. Kelfoun (2008), New methodology for initial volume estimation of Martian landslides from DTM and imagery, paper 8023 presented at Workshop on Martian Gullies: Theories and Tests, Lunar and Planet. Inst., Houston, Tex.
Lucchitta, B. K. (1978), Morphology of Chasma walls, Mars, *J. Res. U. S. Geol. Surv.*, *6*, 651–662.
Lucchitta, B. K. (1979), Landslides in Valles Marineris, Mars, *J. Geophys. Res.*, *84*, 8097–8113.
Lucchitta, B. K. (1987), Valles Marineris, Mars—Wet debris flows and ground ice, *Icarus*, *72*, 411–429.
Lucchitta, B. K., A. S. McEwen, G. D. Clow, P. E. Geissler, R. B. Singer, R. A. Schultz, and S. W. Squyres (1992), The canyon system on Mars, in *Mars*, edited by H. H. Keiffer et al., pp. 453–492, Univ. of Ariz. Press, Tucson, Ariz.
Malin, M. C., and K. S. Edgett (2000), Evidence for persistent flow and aqueous sedimentation on early Mars, *Science*, *302*, 1931–1934.
Malin, M. C., K. S. Edgett, L. V. Posiolova, S. M. McColley, and E. Z. N. Dobrea (2006), Present-day impact cratering rate and contemporary gully activity on Mars, *Science*, *314*, 1573–1577.
Mangeney, A. (2011), Geomorphology: Landslide boost from entrainment, *Nat. Geosci.*, *4*, 77–78.
Mangeney, A., P. Heinrich, and R. Roche (2000), Analytical and numerical solution of the dam-break problem for application to water floods, debris and dense snow avalanches, *Pure Appl. Geophys.*, *157*, 1081–1096.
Mangeney, A., L. Staron, D. Volfson, and L. Tsimring (2006), Comparison between discrete and continuum modeling of granular spreading, in *Proceedings of the 10th WSEAS International Conference on Applied Mathematics*, pp. 63–70, World Sci. and Eng. Acad. and Soc., Stevens Point, Wis.
Mangeney, A., F. Bouchut, N. Thomas, J.-P. Vilotte, and M.-O. Bristeau (2007a), Numerical modeling of self-channeling granular flows and of their levee-channel deposits, *J. Geophys. Res.*, *112*, F02017, doi:10.1029/2006JF000469.
Mangeney, A., L. S. Tsimring, D. Volfson, I. S. Aranson, and F. Bouchut (2007b), Avalanche mobility induced by the presence of an erodible bed and associated entrainment, *Geophys. Res. Lett.*, *34*, L22401, doi:10.1029/2007GL031348.
Mangeney, A., O. Roche, O. Hungr, N. Mangold, G. Faccanoni, and A. Lucas (2010), Erosion and mobility in granular collapse over sloping beds, *J. Geophys. Res.*, *115*, F03040, doi:10.1029/2009JF001462.
Mangeney-Castelnau, A., J.-P. Vilotte, M.-O. Bristeau, B. Perthame, F. Bouchut, C. Simeoni, and S. Yernini (2003), Numerical modeling of avalanches based on Saint Venant equations using a kinetic scheme, *J. Geophys. Res.*, *108*(B11), 2527, doi:10.1029/2002JB002024.
Mangeney-Castelnau, A., F. Bouchut, J. P. Vilotte, E. Lajeunesse, E. Aubertin, and M. Pirulli (2005), On the use of Saint Venant equations to simulate the spreading of a granular mass, *J. Geophys. Res.*, *110*, B09103, doi:10.1029/2004JB003161.
Mangold, N., A. Mangeney, V. Migeon, V. Ansan, A. Lucas, D. Baratoux, and F. Bouchut (2010), Sinuous gullies on Mars: Frequency, distribution, and implications for flow properties, *J. Geophys. Res.*, *115*, E11001, doi:10.1029/2009JE003540.
McEwen, A. S. (1989), Mobility of large rock avalanches: Evidence from Valles Marineris, Mars, *Geology*, *17*, 1111–1114.
Mège, D., and O. Bourgeois (2010), Destabilization of Valles Marineris wallslopes by retreat of ancient glaciers, *Lunar Planet. Sci.*, *XLI*, Abstract 1713.
Mège, D., and P. Masson (1996), Amounts Crustal stretching in Valles Marineris, Mars, *Planet. Space Sci.*, *44*, 749–782.
Melosh, H. J. (1979), Acoustic fluidization: A new geologic process?, *J. Geophys. Res.*, *84*, 7513–7520.
Neukum, G., R. Jaumann, H. Hoffmann, T. Behnke, R. Pischel, T. Roatsch, G. Hauber, E. Arnold, J. Oberst, and HRSC Co-Investigator Team Imaging (2000), Goals and capabilities of the HRSC camera experiment onboard Mars Express, *Lunar Planet. Sci.*, *XXXI*, Abstract 1906.
Peulvast, J. P., and P. L. Masson (1993), Erosion and tectonics in Central Valles Marineris (Mars)—A new morpho-structural model, *Earth Moon Planets*, *61*, 191–217.
Peulvast, J.-P., D. Mège, J. Chiciak, F. Costard, and P. Masson (2001), Morphology, evolution and tectonics of Valles Marineris wallslopes (Mars), *Geomorphology*, *37*, 329–352.
Phillips, J. C., A. J. Hogg, R. R. Kerswell, and N. H. Thomas (2006), Enhanced mobility of granular mixtures of fine and coarse particles, *Earth Planet. Sci. Lett.*, *246*, 466–480.
Pirulli, M., and A. Mangeney (2008), Result of back-analysis of the propagation of rock avalanches as a function of the assumed rheology, *Rock Mech. Rock Eng.*, *41*, 59–84.
Pirulli, M., M. O. Bristeau, A. Mangeney, and C. Scavia (2007), The effect of the earth pressure coefficients on the runout of granular material, *Environ. Modell. Software*, *22*, 1437–1454.
Pouliquen, O. (1999), Scaling laws in granular flows down rough inclined planes, *Phys. Fluids*, *11*, 542–548.
Pouliquen, O., and Y. Forterre (2002), Friction law for dense granular flows: Application to the motion of a mass down a rough inclined plane *J. Fluid Mech.*, *453*, 133–151.
Press, W. H., B. P. Flannery, S. A. Teukolsky, and W. T. Vetterling (1988), *Numerical Recipes in C: The Art of Scientific Computing*, Cambridge Univ. Press, New York.
Pudasaini, S. P., and K. Hutter (2007), *Avalanche Dynamics: Dynamics of Rapid Flows of Dense Granular Avalanches*, Springer, Berlin.
Quantin, C., P. Allemand, and C. Delacourt (2004), Morphology and geometry of Valles Marineris landslides, *Planet. Space Sci.*, *52*, 1011–1022.

Reiche, P. (1937), The Toreva block, a distinctive landslide type, *J. Geol. 45*, 538–548.

Roche, O., M. A. Gilbertson, J. C. Phillips, and R. S. J. Sparks (2004), Experimental study of gas-fluidized granular flows with implications for pyroclastic flow emplacement, *J. Geophys. Res.*, *109*, B10201, doi:10.1029/2003JB002916.

Sassa, K. (1985), The mechanism of debris flows, in *Proceedings of the Eleventh International Conference on Soil Mechanics and Foundation Engineering*, pp. 1173–1176, A. A. Balkema, Rotterdam, Netherlands.

Sassa, K. (1988), Geotechnical model for the motion of landslides (Special lecture), in *Landslides: Proceedings of the Fifth International Symposium on Landslides*, vol. 1, edited by C. Bonnard, pp. 37–56, A. A. Balkema, Rotterdam, Netherlands.

Sato, H., D. Baratoux, K. Kurita, F. Heuripeau, and P. Pinet (2007), Volume measurements of Martian landslides: Accuracy assessment and implications for dynamics, *LPI Contrib.*, *1353*, Abstract 3169.

Savage, S. B., and K. Hutter (1989), The motion of a finite mass of granular material down a rough incline. *J. Fluid. Mech.*, *199*, 177–215.

Schorghofer, N., O. Aharonson, M. F. Gerstell, and L. Tatsumi (2007), Three decades of slope streak activity on Mars, *Icarus*, *191*, 132–140.

Schultz, R. A. (1991), Structural development of Coprates Chasma and western Ophir Planum, Valles Marineris Rift, Mars, *J. Geophys. Res.*, *96*, 22,777–22,792.

Schultz, R. A. (1995) Gradients in extension and strain at Valles Marineris, Mars, *Planet. Space Sci.*, *43*, 1561–1566.

Schultz, R. A. (1998) Multiple-process origin of Valles Marineris basins and troughs, Mars, *Planet. Space Sci.*, *46*, 827–834.

Shaller, P. J. (1991), Analysis and implications of large Martian and terrestrial landslides, Ph.D. thesis, Calif. Inst. of Technol., Pasadena.

Shaller, P. J., B. C. Murray, and A. L. Albee (1989), Subaqueous landslides on Mars?, *Lunar Planet. Sci.*, *XX*, Abstract 990.

Sherard, J. L., R. J. Woodward, S. F. Gizienski, and W. A. Clevenges (1963), *Earth and Earth-Rock Dams*, John Wiley, New York.

Siavoshi, S., and A. Kudrolli (2005), Failure of a granular step, *Phys. Rev. E*, *71*, 051302.

Smart, K. J., D. M. Hooper, and D. W. Sims (2010), Discrete element modeling of landslides in Valles Marineris, Mars, Abstract P51B-1430 presented at 2010 Fall Meeting, AGU, San Francisco, Calif., 13–17 Dec.

Smith, D. E., and M. T. Zuber (1999), The relationship of the MOLA topography of Mars to the mean atmospheric pressure, *Bull. Am. Astron. Soc.*, *31*, 1178.

Sosio, R., G. B. Crosta, and O. Hungr (2008), Complete dynamic modeling calibration for the Thurwieser rock avalanche (Italian Central Alps), *Eng. Geol. Amsterdam*, *100*, 11–26.

Soukhovitskaya, V., and M. Manga (2006), Martian landslides in Valles Marineris: Wet or dry?, *Icarus*, *2*, 348–352.

Stein, A., F. Van der Meer, and B. Gorte (Eds.) (1999), *Spatial Statistics for Remote Sensing*, Kluwer Acad., Dordrecht, Netherlands.

Torson, J. M., and K. J. Becker (1997) ISIS—A software architecture for processing planetary images, *Lunar Planet. Sci.*, *XXVIII*, Abstract 1219.

Voellmy, A. (1955) Über die Zertörungskraft von Lawinen, *Schweiz. Bauztg.*, *73*, 280–285.

F. Bouchut, Laboratoire d'Analyse et de Mathématiques Appliquées, Université Paris-Est, UMR CNRS 8050, Marne la Vallèe F-77454, France.

A. Lucas, California Institute of Technology, Division of Geological and Planetary Sciences, 1200 E. California Blvd., Pasadena, CA 91125, USA. (alucas@caltech.edu)

A. Mangeney, Institut de Physique du Globe de Paris, Université Paris Diderot, UMR CNRS 7154, Paris F-75005, France.

D. Mège, Laboratoire de Planétologie et de Géodynamique, Université de Nantes, UMR CNRS 6112, Nantes F-44000, France.